nature portfolio

https://doi.org/10.1038/s41586-021-04346-w

Supplementary information

Morphogen gradient scaling by recycling of intracellular Dpp

In the format provided by the authors and unedited

SUPPLEMENTARY INFORMATION

1 SUPPLEMENTARY METHODS: Five-compartment model of morphogen transport

This section follows Aguilar-Hidalgo *et al* (2019)[1] and introduces the dynamical equations that capture the trafficking processes discussed throughout the main text. The analysis is based on a discrete cell model for the transport of ligand molecules that are secreted locally at the source and spread along one axis of the tissue, which consists of a row of cells of size a, and specify a morphogen production region of size $(2w + 1)a$ placed in the center of the tissue[1]. We define five pools of molecules as shown in Fig. 1a in the main text. We denote the number of extracellular ligand molecules located between cell n and $n + 1$ and not bound to the internalizing receptors by L_n. The number of ligand molecules bound to receptors at the plasma membrane at the right and left sides of cell n are denoted $S_n^{(r)}$ and $S_n^{(l)}$, respectively. The number of ligand molecules internalized upon receptor binding is denoted $S_n^{(e)}$. Molecules in this pool can be degraded, recycled back to the plasma membrane or transferred to the immobile pool of intracellular molecules denoted $S_n^{(i)}$. The $S_n^{(i)}$ pool can be degraded but does not return to the $S_n^{(e)}$ pool. The different pools of molecules are shown in the diagram on Fig. 1a.

1.1 Dynamic equations

The dynamic equations of the five pool model described above read:

$$\frac{dL_n}{dt} = \frac{D_0}{a^2}(L_{n-1} - 2L_n + L_{n+1}) + k_{off}\left(S_n^{(r)} + S_{n+1}^{(\ell)}\right) - k_{on}L_n + \frac{1}{2}(\nu_n + \nu_{n+1}) \quad \text{(S1.1)}$$

$$\frac{dS_n^{(r)}}{dt} = -\left(k_{off} + k\right)S_n^{(r)} + \frac{k_{on}}{2}L_n + \frac{k_r}{2}S_n^{(e)} \quad \text{(S1.2)}$$

$$\frac{dS_n^{(\ell)}}{dt} = -\left(k_{off} + k\right)S_n^{(\ell)} + \frac{k_{on}}{2}L_{n-1} + \frac{k_r}{2}S_n^{(e)} \quad \text{(S1.3)}$$

$$\frac{dS_n^{(e)}}{dt} = k\left(S_n^{(\ell)} + S_n^{(r)}\right) - k_r S_n^{(e)} - (k_1 + k_i)S_n^{(e)} \quad \text{(S1.4)}$$

$$\frac{dS_n^{(i)}}{dt} = k_i S_n^{(e)} - k_2 S_n^{(i)} \quad \text{(S1.5)}$$

Here the index n with $-N \leq n \leq N$ labels cells in the tissue. Equations (S1.1-S1.5) are valid for L_n if $-N-1 \leq n \leq N$ and for $S_n^{(r,l,e,i)}$ if $-N \leq n \leq N$. Morphogen molecules are produced at a localized source and secreted to contribute to the L_n pool in the extracellular space . The production rate for cell n is given by ν_n and is nonzero only inside the source. Molecules diffuse in the extracellular space with diffusion coefficient D_0. They can bind to the internalizing receptors on the cell membrane at the left and right side of cells with binding rate k_{on}. Bound ligand can unbind with rate k_{off} and can be internalized with rate k into the pool $S_n^{(e)}$. Molecules of the pool $S_n^{(e)}$ are recycled to the extracellular space at rate k_r, are degraded at degradation rate k_1 or transferred to the immobile pool $S_n^{(i)}$ at rate k_i. Finally, the immobile pool is degraded at rate k_2.

It follows from the formulation above that molecules can in principle enter the free extracellular pool through two routes: the secretory pathway or through recycling and receptor unbinding. Secretion only occurs in the source whereas recycling is possible both in the source and the target tissue. These two processes are independent of one another and are as such described by independent terms in Eq. (S1.1-S1.5). Changes in the recycling rate or receptor unbinding may affect the flux of molecules entering the extracellular space, but do not impact on the rate of secretion that depends on transcriptional dynamics at the source. In the analysis that follows in the main text we assume that the secretion rate at the source is constant over time as indicated by experiments that measured the levels of Dpp transcription over time[2].

The balance equation, boundary conditions and dynamics of this theoretical framework are defined in detail in Aguilar-Hidalgo *et al* report[1]. In particular, it can be shown that the dynamics of morphogen transport in this framework are governed by a set of five dynamical modes that capture the dispersal dynamics of the system.

1.2 Steady-state concentration profiles

Equations (S1.1) to (S1.5) can be solved at steady state in a piece-wise manner for regions of constant production rate ν_n. We have $\nu_n = 1$ if the n^{th} cell is cell inside the source and 0 if

not. The steady state solution can be obtained using an exponential Ansatz in the Fourier-Laplace space[1]. This yields an expression for the gradient decay length λ that in the limit of large $\lambda >> a$ can be approximated as,

$$\lambda \approx \left[\frac{D_0}{k_{on}}\left(1+\frac{k_{off}}{k}\left(1+\frac{k_r}{k_i+k_1}\right)\right)+a^2\frac{k_r}{4(k_i+k_1)}\frac{k_{off}}{(k_{off}+k)}\right]^{\frac{1}{2}} \quad \text{(S1.6)}$$

This is the expression for the decay length presented in the main text and used throughout our analysis. Details of the derivation can be found in Aguilar-Hidalgo *et al* report[1].

1.3 Effective diffusion constant and effective degradation rate

Equations (S1.1) to (S1.5) define the dynamics of the five pools of molecules introduced here and in the main text (Fig. 1a), and can be solved to obtain the time dependent solution for the morphogen concentration. Furthermore, the dynamic behaviour of this system is captured by five dynamical modes. Each dynamical mode describes pairs of an effective diffusivity and an effective degradation rate that we denote by D_α and K_α respectively, for $\alpha = 1; 2; \ldots; 5$.

The values of (D_α, K_α) can be expressed as a function of the trafficking rates introduced above. This is achieved using a Fourier representation for the morphogen profiles that leads to an eigenvalue problem which can be solved to obtain the expressions of (D_α, K_α) for $\alpha = 1; 2; \ldots; 5$ [1].

We detail the expressions for (D_α, K_α) in the section that follows. Ultimately, the values of (D_α, K_α) for $\alpha = 1; 2; \ldots; 5$ can be estimated by substituting the parameterized rates we obtained using the experimental assays. This allows us to relate each individual mode to perturbations at different time and length scales. In particular, we find that the fourth mode (D_4, K_4) dominates the dynamics of the FRAP experiment. Therefore the fourth mode could in principle help us understand the clusters of solutions obtained numerically in the FRAP assay.

1.3.1 Effective degradation rates and effective diffusivities

The effective degradation rates are given by:

$$K_1 = -\frac{1}{3}\left(a_2 - 2\sqrt{\Delta_0}cos\left(\frac{1}{3}arccos - \frac{\Delta_1}{2\sqrt{\Delta_0}}\right)\right) \quad \text{(S1.7)}$$

$$K_2 = k_{off} + k \tag{S1.8}$$

$$K_3 = -\frac{1}{3}\left(a_2 - 2\sqrt{\Delta_0}cos\left(\frac{1}{3}arccos - \frac{\Delta_1}{2\sqrt{\Delta_0}} - \frac{2\pi}{3}\right)\right) \tag{S1.9}$$

$$K_4 = -\frac{1}{3}\left(a_2 - 2\sqrt{\Delta_0}cos\left(\frac{1}{3}arccos - \frac{\Delta_1}{2\sqrt{\Delta_0}} - \frac{4\pi}{3}\right)\right) \tag{S1.10}$$

$$K_5 = k_2 \tag{S1.11}$$

where $K_1 > K_2 > K_3 > K_4 > K_5$ and with

$$\Delta_0 = a_2^2 - 3a_1 \tag{S1.12}$$

$$\Delta_1 = 2a_2^3 - 9a_2a_1 + 27a_0 \tag{S1.13}$$

and

$$a_2 = -\left(k_r + k_i + k_1 + k + k_{off} + k_{on}\right) \tag{S1.14}$$

$$a_1 = (k_r + k_i + k_1)\left(k_{off} + k_{on}\right) + k(k_i + k_1 + k_{on}) \tag{S1.15}$$

$$a_0 = -kk_ok_{on} \tag{S1.16}$$

We now provide expressions for the diffusivities associated to the five modes. First, the mode with effective degradation $K_5 = k_2$ is a non-diffusive mode and

$$D_5 = 0 \tag{S1.17}$$

This mode dominates the dynamics in the immobile pool where molecules degrade at rate k_2 and do not disperse. The remaining diffusion coefficients are given by:

$$D_\alpha = \frac{-\sigma_0 + D_0(K_\alpha^3 - \sigma_1 K_\alpha^2 + \sigma_2 K_\alpha - \sigma_3)}{\prod_{\substack{\beta=1 \\ \beta\neq\alpha}}^{4}(K_\alpha - K_\beta)} \tag{S1.18}$$

for α = 1; 2; 3; 4

where

$$\sigma_0 = \frac{a^2}{4}k_rkk_{on}k_{off} \tag{S1.19}$$

$$\sigma_1 = k_r + k_i + k_1 + 2\left(k_{off} + k\right) \tag{S1.20}$$

$$\sigma_2 = \left(k_{off} + k\right)\left(k + k_{off} + 2(k_i + k_1)\right) + \left(2k_{off} + k\right)k_r \tag{S1.21}$$

$$\sigma_3 = \left(k_{off} + k\right)\left((k_r + k_i + k_1)k_{off} + kk_o\right) \quad \text{(S1.22)}$$

The expressions for (D_α, K_α) given here can in principle be used *a posteriori* to understand the spatial pattern of the parameter distributions projected on the different planes as described in the main text and chapter 2.5.2.

2 SUPPLEMENTARY METHODS : Assays

2.1 Parameterisation assay 1: Steady-state decay length of the GFP-Dpp gradient

2.1.1 Measurement of the steady-state gradient profile

In order to determine the decay length of the Dpp gradient, we imaged GFP-Dpp fluorescence profiles in wing discs from transgenic animals where the GFP-Dpp fusion is expressed under the control of the LOP expression system from its endogenous domain as previously described [3]. This drives GFP-Dpp expression at levels which are similar to those of endogenous Dpp ([3]; see also Extended Data Fig. 3a for Western blot analysis of the expression levels) in contrast to overexpression by more than 10-fold with the previously used Gal4 system. It is worth noting that these GFP-Dpp^{LOP} expressing animals have previously been shown to reach adulthood in a Dpp mutant background[3], implying that GFP-Dpp^{LOP} recapitulates the distribution and dynamics of endogenous Dpp.

2.1.2 Steady-state gradient profile and gradient scaling analysis

Quantification of steady-state spatial profiles of eGFP-Dpp or P-Mad has been performed in the posterior compartment and orthogonal to the source, averaging over more than two cell diameters (above 6 µm) in the y axis (as previously described[2]). The fixation, mounting and imaging conditions were the same for all discs of a given dataset. eGFP-Dpp or P-Mad spatial profiles were quantified with ImageJ from maximum projections of z-stacks comprising the apical most 10 µm of the wing disc epithelium, where most of the GFP-Dpp signal is present[2,4]. In order to estimate the decay length λ, the spatial profiles have been fitted by a single exponential function with an offset (previously described[2]). Gradient scaling analysis has been performed as previously described[2] on intensity profiles after offset subtraction (Extended Data Fig. 6p) and consists of (i) evaluating the proportionality of the decay length λ of eGFP-Dpp^{LOP} gradients and the posterior compartment length ℓ for discs of different sizes (see scaling plots in Fig. 2a and Extended Data Fig. 7c,f; 8a,b) and (ii) evaluating the collapse of normalized gradients of discs of different sizes onto a single profile (shown for eGFP-Dpp^{LOP} in Extended Data Fig. 6p-r).

Scaling plots represent the decay length λ determined from an exponential fit to the spatial profiles of eGFP-Dpp or pMad plotted as a function of the posterior compartment length ℓ. The slope ϕ of the linear regression is a measure for the quality of scaling (Extended Data Fig.

7c,f; 8a,b). As seen from the scaling plots in Extended Data Fig. 7c,f; 8a,b, in *pent*^{2} and *dally*^{gem} mutant discs, eGFP-Dpp or P-Mad gradients scale poorly: as the wing grows and ℓ increases, λ remains approximately invariant and ϕ is very small. Note that, in all these cases, ϕ determined from the data in scaling mutant discs is significantly different from ϕ determined from the data in control discs.

To study the gradient shape, Dpp concentration profiles were normalized with respect to the posterior compartment length ℓ and the gradient amplitude C_0 (Extended Data Fig. 6q,r) that was estimated for each individual gradient profile by an exponential fit (Extended Data Fig. 3g). The quality of fit has been confirmed by plotting the residuals of exponential fit (Extended Data Fig. 3h,i). For the density plots (Extended Data Fig. 6r), the fraction of the total number of normalized gradients of all stages passing through any particular $r, C(r)/C_0$ bin was calculated and color-coded (r, relative position; $C(r)/C_0$, fluorescent signal normalized to C_0) as previously described [2].

In this report we perform the parameterization of transport rates of eGFP-Dpp^{LOP} in large discs of posterior compartment size $\ell = 144.6 \pm 11.9\ \mu m$ and small discs of posterior compartment size $\ell = 79.3 \pm 2.8\ \mu m$ (average $\pm$ standard deviations). The choice of sizes is motivated by the fact that the smallest discs in which the assays can reliably be performed are about 80 μm and in discs larger than 144 μm, the amplitude of the Dpp gradients start normally a rapid decrease in preparation for pupariation. In the following assays (namely, the nanobody uptake assay, the extracellular fraction determination assay, the long-term FRAP assay and the conventional FRAP assay), for the conditions $\ell = 144\ \mu m$ and $\ell = 80\ \mu m$, discs have been chosen of posterior length within the standard deviations given above (11.9 and 2.8 respectively).

***Background substraction*.** When measuring Dpp gradients, we considered background in three different ways: i) by measuring the fluorescence at the edge of the corresponding gradient, ii) by estimating background as a fitted offset parameter in the exponential fit to the gradient and (iii) linear unmixing analysis[5]. This analysis showed that substracting the measured background at the edge is equivalent to linear unmixing. This is because of two reasons: i) background is largely homogeneous in the disc, and ii) the length of the posterior compartment is ten-fold longer (approximately) than the decay length of the gradient (unlike the case of the Bicoid gradient, which is only half of the length of the embryo approximately). Therefore, fluorescence at the edge of the disc is background.

2.2 Parameterisation assay 2: Nanobody internalization assay

2.2.1 Theory of the nanobody internalization assay

In the nanobody uptake experiment, live eGFP-Dpp^{LOP}-expressing discs are incubated in a GBP-Alexa555 solution (Extended Data Fig. 3n). The fluid phase internalization of GBP-Alexa555 is negligible in our experimental setup (see below, Extended Data Fig. 3o,p): the nanobody can only be internalized into the cells by binding to eGFP-Dpp^{LOP}. We therefore are specifically following the trafficking of the complex GBPAlexa555-eGFP-Dpp^{LOP}. The affinity of the nanobody to GFP is very high (dissociation constant of 1 pM, Chromotek), hence all extracellular eGFP-Dpp^{LOP} molecules (whether bound to the membrane or not) are labelled by GBP-Alexa555 in a very short time scale. Therefore, for simplicity we consider the binding to be instantaneous.

To describe the dynamics of the nanobody internalization assay, we consider the theoretical framework of the five-compartment model introduced in Section 1. We define the different pools of molecules:

- GFP-Dpp molecules not bound to the nanobody in the extracellular space (concentration u), in the endosomal pool (u_e) and in the immobile pool (u_i).
- GFP-Dpp molecules bound to the nanobody in the three pools (concentrations c, c_e and c_i, respectively).
- Total concentration of GFP-Dpp molecules whether bound or not (g, g_e and g_i).
- Total nanobody concentration whether bound or not to GFP-Dpp (n, n_e and n_i).

Because of the high affinity of the nanobody, its quasi-instantaneous binding to GFP and the fact that the nanobody is in sufficient amounts, we consider that $u = 0$ and $c = g$ (i.e. the GFP-Dpp extracellular pool is fully bound to the nanobody). Also c is constant in time for the duration of the assay, reflecting that the concentration in the extracellular space is at quasi-steady-state.

To establish the proper concentration of nanobody in our incubation solution, we have performed the nanobody uptake experiment using solutions with increasing concentration of GBP-Alexa555 (data not shown). We studied how increasing concentrations of GBP-Alexa555 affects the fluorescence signal at the beginning of the experiment, which corresponds to the total amount of the nanobody in the intercellular space at $t = 0$. We find that the extracellular fluorescence signal only increases with the GBP-Alexa555 concentration in the

solution for low concentrations of GBP-Alexa555. Above a threshold (0.04 μM), no further increase in the intercellular fluorescence is observed, indicating that above this threshold, nanobody and GFP-Dpp are in comparable amounts (i.e. $n \approx c$) in the measured ROI. We used this threshold concentrations for our experiments.

The equations for the dynamics of the labelled and unlabelled GFP-Dpp pools are,

$$\partial_t c_e = k_N c - (k_i + k_r + k_1) c_e \qquad \text{(S2.1)}$$

$$\partial_t c_i = k_i c_e - k_2 c_i \qquad \text{(S2.2)}$$

$$\partial_t u_e = -(k_i + k_r + k_1) u_e \qquad \text{(S2.3)}$$

$$\partial_t u_i = k_i u_e - k_2 u_i \qquad \text{(S2.4)}$$

We can solve equations (S2.1) and (S2.2) to obtain the time dependent solutions for c_e and c_i. The solutions read,

$$c_e(t) = \frac{k_N c}{k_i + k_r + k_1}\left(1 - e^{-(k_i + k_r + k_1)t}\right) \qquad \text{(S2.5)}$$

$$c_i(t) = \frac{k_N k_i c}{k_i + k_r + k_1 - k_2}\left(\frac{1 - e^{-k_2 t}}{k_2} - \frac{1 - e^{-(k_i + k_r + k_1)t}}{k_i + k_r + k_1}\right) \qquad \text{(S2.6)}$$

The total concentration of nanobody labelled GFP-Dpp is the sum of $c_e(t)$ and $c_i(t)$ given in equations (S2.5) and (S2.6). Recall however that the fluorophore of the nanobody (Alexa555) is not degraded due to the absence of hydrolases that can metabolize this exogenous compound in the lysosome. It follows that in our experiment, we are also detecting Alexa555 signal after GFP-Dpp itself was already degraded. To account for this, we derive the dynamics of the total A555 signal in the endosomal and immobile pools, n_e and n_i, and compute $\delta n_e = n_e - c_e$ and $\delta n_i = n_i - c_i$, where δn_e and δn_i capture the accumulation of the A555 signal due to the absence of degradation. The dynamics of n_e, n_i, δn_e and δn_i are described by,

$$\partial_t n_e = k_N c - (k_i + k_r) c_e \qquad \text{(S2.7)}$$

$$\partial_t n_i = k_i c_e \qquad \text{(S2.8)}$$

$$\partial_t \delta n_e = k_1 c_e \qquad \text{(S2.9)}$$

$$\partial_t \delta n_i = k_2 c_i \qquad \text{(S2.10)}$$

We can now solve for δn_e and δn_i by substituting equations (S2.5) and (S2.6) in (S2.9) and (S2.10), respectively. The time dependent solutions for δn_e and δn_i are then given by,

$$\delta n_e(t) = \frac{k_1 k_N c}{k_1+k_r+k_i} t + \frac{k_1 k_N c}{(k_i+k_r+k_1)^2}\left(e^{-(k_i+k_r+k_1)t} - 1\right) \quad \text{(S2.11)}$$

$$\delta n_i(t) = \frac{k_N k_i c}{k_i+k_r+k_1-k_2}\left(t - \frac{e^{-k_2 t}-1}{k_2}\right) - \frac{t}{k_i+k_r+k_1} - \frac{1}{(k_i+k_r+k_1)^2}\left(e^{-(k_i+k_r+k_1)t} - 1\right) \quad \text{(S2.12)}$$

The dynamics of the total nanobody concentration is given by,

$$n_{tot} = n + c_e + \delta n_e + c_i + \delta n_i \qquad \text{(S2.13)}$$

We can now substitute equations (S2.5), ((S2.6), (S2.11) and (S2.12) in equation (S2.13) to obtain the following expression for the total nanobody concentration as a function of the kinetic parameters,

$$n_{tot}(t) = n + \frac{k_N c}{k_i+k_r+k_1}\left[\frac{k_r}{k_i+k_r+k_1}\left(1 - e^{-(k_i+k_r+k_1)t}\right) + (k_i + k_1)t\right] \qquad \text{(S2.14)}$$

It follows that the total nanobody concentration obeys the following phenomenological equation,

$$C_T^i(t) = C^i(1 + B(1 - e^{-pt}) + At) \qquad \text{(S2.15)}$$

where $\mathrm{n} = \mathrm{c} = \mathrm{C^i}$ is the extracellular concentration of the nanobody bound to GFP-Dpp at the beginning of each experiment. This phenomenological equation captures extremely well the dynamics of Alexa555 accumulation observed experimentally (Extended Data Fig. 3k,l). In this equation, A, B and p are given by,

$$A = k_N - k_r k_N/(k_o + k_r) \qquad \text{(S2.16)}$$

$$B = k_r k_N/(k_o + k_r)^2 \qquad \text{(S2.17)}$$

$$p = k_o + k_r \qquad \text{(S2.18)}$$

Where $\mathrm{k_o} = \mathrm{k_i} + \mathrm{k_1}$. We can fit expression (S2.15) to the experimental data (see chapter 2.2.3) to obtain A, B and p and can retrieve $\mathrm{k_r}$, $\mathrm{k_N}$ and $\mathrm{k_o}$using,

$$k_r = p^2 B/(pB + A) \qquad \text{(S2.19)}$$

$$k_N = pB + A \qquad \text{(S2.20)}$$

$$k_o = k_i + k_1 = p - k_r \qquad \text{(S2.21)}$$

Finally, note that the internalization rate used in the above derivation, k_N, is not the same as the rate of endocytosis in the 5-compartment model introduced in Section 1. The nanobody experiment does not distinguish the free extracellular GFP-Dpp *versus* the extracellular bound GFP-Dpp molecules. It follows that the internalization rate captured by the nanobody internalization assay is a composite rate that depends on k (the rate of endocytosis), k_{on} and k_{off}. In a binding equilibrium, k_N is related to k, $\mathrm{k_{on}}$ and $\mathrm{k_{off}}$ by

$$k_N = k\left(\frac{k_{on}}{k_{on}+k_{off}}\right) \qquad \text{(S2.22)}$$

2.2.2 Experimental procedure of the nanobody internalization assay

Discs expressing eGFP-Dpp^{LOP} were mounted on a fluorodish in a fibrinogen clot (see above). Before incubation with the nanobody, an image was taken at 25°C. Temperature in the dish was measured directly by a thermocouple (imaged using Zeiss 780 microscope, 63x objective NA1.4, the temperature is controlled by a Tokai Hit chamber). Discs were then incubated with a GBP-Alexa555 solution (0.04 µM in Clone 8 medium) on ice for 35 minutes to ensure that all extracellular eGFP-Dpp^{LOP} molecules are bound by the GBP-Alexa555. The disc was then transferred back to 25°C and images were taken every 2 minutes (for 15 minutes) and then every 4 minutes (until 6000s).

In order to control that the assay monitors the trafficking of eGFP-Dpp^{LOP} specifically, we have confirmed that the internalized pool of GBP-Alexa555 forms a spatial gradient similar to eGFP-Dpp^{LOP} (Extended Data Fig. 3u,v). Moreover, the internalization of GBP-Alexa555 by fluid phase in wildtype animals without eGFP-Dpp^{LOP} expression was negligible (Extended Data Fig. 3o,p) and the low levels detected are uniform in space (Extended Data Fig. 3q), whereas the internalized pool of nanobody forms a spatial gradient similar to eGFP-Dpp^{LOP} itself (Extended Data Fig. 3u,v). This confirms that the passive internalization of the nanobody by fluid phase is negligible.

We observed that the dynamics of accumulation of Alexa555 fluorescence follows an exponential relaxation to a linear regime (Extended Data Fig. 3k,l). The dynamic equations for the five pools generate such exponential *plus* linear behavior, if we consider the experimental observation that lysosomal degradation of the Alexa555 fluorophore is negligible during the time scale of the assay. This is due to the absence of hydrolase enzymes in the lysosome which

could degrade this artificial compound. Consistent with this, in wildtype discs incubated with the Alexa555 fluorophore, the accumulation of Alexa555 fluorescence follows linear dynamics and does not relax to a plateau in the timescale of our experiment (above 6000s) (Extended Data Fig. 3s,t).

Indeed, the late regime is linear, without saturation, because of the continuous accumulation of fluorophore molecules in the intracellular compartments. The exponential relaxation occurs at a time scale which corresponds to the dwell time $1/(k_r + k_1 + k_i)$ of molecules in the endosomal pool S_e (see also chapter 2.2.1 for the theory of this assay for details).

The dynamics of this low fluid phase internalization is linear: it does not present the initial exponential dynamics seen in the internalization of GFP-Dpp (Extended Data Fig. 3r). This confirms that the fluid phase internalization of GBP-Alexa555 is negligible in our experimental setup and that the exponential behaviour of the dynamics (a signature of recycling) is specific of the trafficking of Dpp.

2.2.3 Nanobody uptake quantification

GBP-Alexa555 fluorescence intensity has been measured in a rectangular ROI with dimensions 10 µm x 200 µm in the posterior compartment adjacent to the Dpp source and with the long side parallel to the source (Fig. 2b-d). Background fluorescence is defined as the signal in the ROI in the image before GBP-Alexa555 incubation of discs. Background fluorescence was subtracted from the fluorescent signal in the images after GBP-Alexa555 incubation. As a quality control for the health of the primary culture, we have measured the gradient of eGFP-Dpp^{LOP} in order to confirm that its decay length is consistent with its posterior width, ℓ.

We obtain the values of k_N, k_o and k_r by fitting the nanobody data to the phenomenological equation (S2.15) derived in chapter 2.2.1 (Extended Data Fig. 3k-m, Fig. 2f). We perform a single fit to all *n* experiments in each condition, since the phenomenological parameters A, B and p are shared between all discs of the same genetic background and size pool. We allow variations in the values of C^i between discs, which captures the total amount of Dpp in the extracellular pool and varies between experiments. By fitting many traces simultaneously, we reduce the number of fit parameters and so degrees of freedom and obtain more reliable parameter estimates.

Our fitting routine entails one degree of degeneracy because an overall amplitude of the parameter C^i depends on A and B (equation (S2.15)), but not their ratio A/B. This introduces an uncertainty in the fit value of k_N, but not on k_o and k_r, equations (S2.19)-(S2.21). Two experimental constraints restrict the value of C^i. First, C^i cannot be lower than the concentration measured at the first time point in each experiment. Second, the value of k_N is proportional to both A and B and so proportional to C^i. k_N represents an upper limit for the rate of endocytosis which cannot be faster than 10s, according to the literature on endocytosis. There is therefore an upper limit in the value of C^i imposed by the upper limit in the rate of endocytosis.

This method makes the fitting routine stringent and allows us to obtain values for A, B and p with relatively tight confidence intervals (see Extended Data Table 2). We use Equations ((S2.19)-(S2.21) to obtain estimates and confidence intervals for (k_N, k_o, k_r) from the fitted values and confidence intervals of A, B and p. These narrow intervals were used as a uniform prior distribution in the Approximate Bayesian Computation method for the remaining parameters (see chapter 2.5.2).

2.3 Parameterisation assay 3: Extracellular fraction determination

We previously estimated the fraction of extracellular Dpp molecules to be about 15% of the total. This was done using a mask based on a membrane marker to discriminate between the extracellular and intracellular fractions of eGFP-Dpp [4]. This previous assay presents two caveats: i) it is not clear whether the molecules in the mask are only extracellular, because of the resolution limits of light microscopy, and ii) the extracellular signal is faint, making a precise measurement very challenging.

Because the accurate determination of the extracellular fraction is important to discriminate between transport regimes, we developed a new assay which addresses these two limitations. We performed a eGFP-Dpp^{LOP} immunostaining which detects the extracellular pool specifically by incubating living wing discs with anti-GFP nanobodies at 4˚C without permeabilization (see also chapter 2.3.2 for further details and control; Extended Data Fig. 1e-i). This labels the extracellular pool exclusively as measured by a functional assay, avoiding the limitations of using a mask (Extended Data Fig. 4g). In this way we can quantify the extracellular pool of eGFP-Dpp^{LOP} (Alexa555 fluorescence) at the same time as the total pool (GFP fluorescence). In our imaging conditions, in equimolar amounts, the nanobody-Alexa555

fluorescent signal is 4.5 fold brighter than the GFP signal. This allows us to obtain a bright fluorescence signal for the extracellular pool and therefore to quantify it robustly (Extended Data Fig. 4g and Fig. 2g). For large discs of $\ell = 144\mu m$ of averge posterior compartment length, the extracellular fraction is $\rho = 0.13 \pm 0.01$ (Fig. 2g), consistent with the value obtained using the extracellular mask method [4]. The extracellular fraction depends on the rates of transport (see equation in Extended Data Fig. 4h) and therefore its actual experimental value constrains the plausible parameter ranges (Extended Data Fig. 4j,k).

2.3.1 Theory of the extracellular fraction ρ

Using the theoretical framework with five pools, we define the extracellular fraction of Dpp at steady state, ρ, as

$$\rho = \frac{L_n + S_n^{(r)} + S_n^{(l)}}{L_n + S_n^{(r)} + S_n^{(l)} + S_n^{(e)} + S_n^{(i)}} \qquad \text{(S2.23)}$$

Where L_n, $S_n^{(r)}$, $S_n^{(l)}$, $S_n^{(e)}$ and $S_n^{(i)}$ are the unbound extracellular pool, bound right and left extracellular pools, endosomal pool and immobile pool of the nth cell, respectively, as defined in the SI 1.1. The relative magnitude of each pool at steady-state is given by equations (S1.1)-(S1.5) in SI 1.1. We use these expressions at the large decay length limit to obtain an estimate for the extracellular fraction given by,

$$\rho = \left(1 + \frac{k_{on} k (1 + k_i/k_2)}{(k_{on} + k_{\text{off}})(k_r + k_o) + k k_o}\right)^{-1} \qquad \text{(S2.24)}$$

The full expression for ρ without the assumption of a large decay length (like in smaller discs) is given by,

$$\rho = \frac{k_2\left(k_0\left(2e^{\frac{1}{\bar{\lambda}}}k + 2e^{\frac{1}{\bar{\lambda}}}k_{off} + (1 + e^{\frac{1}{\bar{\lambda}}})k_{on}\right) + (2e^{\frac{1}{\bar{\lambda}}}k_{off} + (1 + e^{\frac{1}{\bar{\lambda}}})k_{on})k_r\right)}{\left(1 + e^{\frac{1}{\bar{\lambda}}}\right)k k_i k_{on} + k_2\left(k_o\left(2e^{\frac{1}{\bar{\lambda}}}k + 2e^{\frac{1}{\bar{\lambda}}}k_{off} + \left(1 + e^{\frac{1}{\bar{\lambda}}}\right)k_{on}\right) + 2e^{\frac{1}{\bar{\lambda}}}k_{off}k_r + \left(1 + e^{\frac{1}{\bar{\lambda}}}\right)k_{on}(k + k_r)\right)}$$

Where $\bar{\lambda} = \lambda/a$ with λ the dimensional decay length and a the cell size.

We have checked whether the assumption of a large decay length would introduce a considerable error to our estimation of ρ and found that this would not be the case. In particular, the expected error in the three experimental conditions we have considered in our analysis (large, small and *pentagone* mutant discs) give an error below 2%.

2.3.2 Experimental procedure for the extracellular fraction determination

Extracellular staining. To determine the extracellular fraction ρ experimentally, an extracellular eGFP-Dpp^{LOP} immunostaining was performed: living wing discs were incubated with GBP-Alexa555 (0.08 µM) in Clone 8 medium at 4˚C for 60 minutes. They were then extensively washed and fixed with 4% PFA. This procedure labels exclusively the extracellular eGFP-Dpp^{LOP} molecules accessible to the nanobody without permeabilization (Extended Data Fig. 4g). Indeed, GBP-Alexa555 fluorescence is efficiently removed after stripping of the extracellular eGFP-Dpp^{LOP}-bound GBP-Alexa555 molecules by the acid wash (Extended Data Fig. 1e-h). Fixed discs were then imaged using a Zeiss 780 microscope.

Calibration of eGFP to Alexa555 fluorescence. In order to quantify the extracellular pool of eGFP-Dpp^{LOP} (Alexa555 fluorescence) and the total pool (GFP fluorescence) simultaneously, we have calibrated the Alexa555 fluorescence signal and the GFP fluorescence signal to each other. For the calibration, we have used solutions of purified GBP-Alexa555 and eGFP in equimolar amounts. The concentration of these solutions has been determined by the BCA assay (PierceTM BCA Protein Assay Kit, ThermoFisher Scientific). Solutions of equimolar amounts of eGFP and GBP-Alexa555 have been imaged in the microscope in a 348-well plate using identical imaging conditions to those used for the imaging of the extracellular staining of eGFP-Dpp^{LOP}. Images were taken in 5 different positions in the xy plane in a multi-well plate, 150 µm away from the bottom to avoid the reflexion of the glass. We used this procedure to estimate the calibration factor f using the equation below:

$$f = \frac{GFP}{A555} \qquad \text{(S2.25)}$$

Where GFP is the fluorescence signal of the GFP solution and $A555$ is the fluorescence signals of Alexa555 fluorophore of the GBP-Alexa555 solution at equimolar amounts. We have estimated the calibration factor $f = 0.22 \pm 0.02$ (n=20 in 2 experiments).

Equimolarity of GBP-Alexa555 and eGFP in the calibration procedure. After we have determined the concentrations of the GBP-Alexa555 and eGFP solutions by the BCA method and generated equimolar solutions**,** we confirmed this equimolarity by measuring the change of GFP fluorescence in solutions with increasing amounts of GBP-Alexa555 (see Extended Data Fig. 4i). We had noticed that binding of GBP-Alexa555 to eGFP molecules causes a decrease in the eGFP fluorescence intensity (Extended Data Fig. 4i). This is in contrast to the behaviour of the GBP nanobody by itself, which has been reported to boost the fluorescence

of GFP if not coupled to the Alexa555 fluorophore (reference[6] and then also reference[7]). Therefore, in the absence of GBP-Alexa555, eGFP shows its maximal fluorescence. As the relative amount of GBP-Alexa555 increases, an increasing amount of eGFP molecules is quenched, leading to a decrease in the overall GFP fluorescence intensity of the solution (Extended Data Fig. 4i). eGFP fluorescence reaches a minimum value when GBP-Alexa555 is added at equimolar amounts to eGFP: every molecule of eGFP in the solution binds a GBP-Alexa555 molecule and its fluorescence is decreased by a factor. Adding more GBP-Alexa555 molecules than eGFP molecules will not affect the eGFP fluorescence intensity of the solution once all the eGFP molecules are bound. Therefore, the relative concentration of eGFP and GBP-Alexa555 can be determined from the minimal relative concentration at which the minimum value (r_{min}) of eGFP fluorescence has been reached (Extended Data Fig. 4i).

Determination of the fraction E of eGFP fluorescence decrease upon GBP-Alexa555 binding. Binding of GBP-Alexa555 to eGFP molecules reduces their fluorescence intensity. In order to determine the fraction *E* of eGFP fluorescence decrease upon binding of GBP-Alexa555, we have measured the fluorescence of eGFP alone *versus* the fluorescence of eGFP bound to GBP-Alexa555. Solutions of equimolar amounts of eGFP and GBP-Alexa555 *versus* eGFP alone at the same concentration have been imaged in the microscope in a 348-well plate using identical imaging conditions to those used for the imaging of the extracellular staining of eGFP-Dpp^{LOP}. GFP was imaged in 5 different positions in the xy plane in a multi-well plate, 150 µm away from the bottom to avoid the reflexion of the glass. The fraction *E* can be estimated using the equation (S2.26):

$$E = 1 - \frac{GFP_B}{GFP} \qquad \text{(S2.26)}$$

Where GFP and GFP_B is the fluorescence signal of the GFP alone and bound to GBP-Alexa555, respectively. We have determined the fraction $E = 0.81 \pm 0.01$.

Extracellular specificity. In order to confirm that the extracellular staining protocol labels exclusively eGFP-Dpp^{LOP} molecules in the extracellular pool, we have performed an acid stripping after the extracellular staining prior to fixation (Extended Data Fig. 1e-h). Indeed, the GBP-Alexa555 fluorescence signal is largely eliminated after the stripping (91% of GBP-Alexa555 fluorescence is removed).

2.3.3 Quantification of the extracellular staining

We perform an extracellular staining of discs expressing eGFP-Dpp^{LOP} with GBP-Alexa555, as described above. GBP-Alexa555 labels eGFP-Dpp^{LOP} molecules in the extracellular pools (bound and unbound), whereas the green fluorescence of GFP in eGFP-Dpp^{LOP} labels the extracellular and intracellular pools, the total pool. It is important to consider the relative fluorescence signal of GFP *versus* Alexa555 and that, upon binding of the GBP-Alexa555 nanobody to eGFP-Dpp, the GFP fluorescence is partially quenched. Because the GBP-Alexa555 nanobody only binds extracellularly, the quenching only affects the extracellular pool of eGFP-Dpp.

We determine experimentally the ratio ρ of the extracellular to the total pool of eGFP-Dpp as

$$\rho = \frac{C_E}{C_E + C_I} \qquad \text{(S2.27)}$$

where C_E and C_I are the extracellular and intracellular amounts of eGFP-Dpp, respectively. The extracellular amount of eGFP-Dpp can be determined based on the extracellular staining of eGFP-Dpp using the fluorescent signal of the GBP-A555 nanobody and the calibration of GFP *versus* Alexa555 fluorescent signal:

$$C_E = \alpha \cdot A555 \cdot f \qquad \text{(S2.28)}$$

where α is a proportionality factor between GFP fluorescence signal and GFP amount, $A555$ is the fluorescence signal of the A555 fluorophore and f is the calibration factor between GFP and A555 fluorescence signal (see chapter 2.3.2 above).

The intracellular amount of eGFP-Dpp can be determined based on the total amount of eGFP fluorescence, the calibration of GFP *versus* Alexa555 fluorescent signal and the quenching factor caused by nanobody binding to the extracellular (but not intracellular) pool as

$$C_I = \alpha(GFP_T - A555 \cdot f \cdot (1 - E)) \qquad \text{(S2.29)}$$

where GFP_T is the total GFP fluorescence, and $A555 \cdot f \cdot (1 - E)$ corresponds to the estimated fluorescence of the extracellular GFP, taking into account the GFP/A555 calibration and the quenching of the extracellular GFP fluorescence by a factor E (see chapter 2.3.2 above).

From this,

$$\rho = \frac{C_e}{C_e + C_i} = \frac{A555 \cdot f}{GFP_T + A555 \cdot f \cdot E} \qquad \text{(S2.30)}$$

Exponential functions were fitted to graded spatial profiles of GBP-Alexa555 and eGFP. We have used the amplitudes of the exponentials to estimate $A555$ and GFP_T.

2.4 Parameterisation assay 4: long-term FRAP assay

In order to estimate the slow dynamics of degradation from the immobile pool (k_2), we adapted the FRAP assay below (see chapter 2.5) to long time scales (10 hours, Extended Data Fig. 2k-n,q). While in conventional FRAP (see below) images are taken every 2-5 minutes during 1h, in the long-term FRAP, the interval between images is 20 minutes for 10h to avoid phototoxicity and photobleaching.

The relaxation time of the slow dynamics (k_{IF}) can be estimated in two different ways:

1) fitting a double exponential to the entire recovery curve: the early (before 45 minutes of recovery) fast mobile pool dynamics and the late (after 45 minutes of recovery) slow immobile pool dynamics (Extended Data Fig. 2l)
2) fitting a single exponential with an offset to the recovery of only the late slow immobile pool dynamics (Extended Data Fig. 2m). In this case, the offset corresponds to the fraction of Dpp molecules in the mobile pool (mobile fraction) as determined by the conventional FRAP assay (see below, chapter 2.5).

The immobile pool relaxation is slower than the growth rate (see chapter 2.9, Extended Data Figure 2q) and is therefore not in steady-state. The slow dynamics seen in the long-term FRAP experiment (k_{IF}) is therefore composed of the contribution of both the immobile pool relaxation (k_2) and the relaxation caused by growth (g; growth rate, causing advection and dilution). The parameter k_2 is therefore given by: $k_2 = k_{IF} - g$ (Extended Data Figure 2o-q). The value of k_2 is similar in small and large discs.

Note that the value of k_2 estimated with the long-term FRAP assay is similar to the value estimated previously in Entchev *et al*.[8]. In the Entchev report, using temporal control of GFP-Dpp transcription, a pulse of Dpp secretion was generated and the formation of the gradient was followed at long time scales. After four hours, recovery of the gradient was partial, whereas after eight hours, it was complete[8].

The value of the degradation rate of the immobile fraction k_2 is constrained by the time scale of recovery of the full gradient (which includes the immobile fraction). The rate k_o is related to the relaxation of the mobile fraction in the FRAP assay. Because the time scales of recovery of the two fractions (mobile and immobile) are different, k_2 must be smaller than k_o.

2.5 Parameterisation assay 5: Fluorescence Recovery After Photobleaching (FRAP)

2.5.1 Experimental procedure

Fluorescence Recovery After Photobleaching (FRAP) experiments have been performed on discs expressing eGFP-Dpp^{LOP}. Live discs were mounted on a fluorodish in a fibrinogen clot in order to immobilize and keep the tissue healthy during the experiment. In this healthy tissue, more than 50% of the GFP-Dpp fluorescence recovers within 90 minutes. This is the so-called mobile fraction. Indeed, a substantial level of recovery indicates that the transport mechanisms are intact in this experiment, in contrast to very small mobile fractions (20%) in previous reports [9].

The imaging and photobleaching were performed with the FRAP module of the SP8 microscope using the following setup: 1024x1024, frequency of 100Hz, 2.6 Airy Units, 100% 488nm laser, scan field reduced to the bleach region during photobleaching, bleach format changed to reduce the number of scanned lines two fold. These settings resulted in a bleaching time of 623 msec per iteration. Fifty bleaching iterations have been performed. GFP-Dpp^{LOP} fluorescence was photobleached in a region of interest (ROI) adjacent and parallel to the Dpp source in the posterior compartment (a rectangular stripe of width of 10 µm; see Extended Data Fig. 4a). The fluorescence intensity of eGFP-Dpp^{LOP} in the ROI has been imaged as a function of time: images were taken with a time interval of 140s (first 3 timepoints) and then with time intervals of 280s for the subsequent hour. The temperature was maintained at 25°C (as measured by a thermocouple directly in the dish) using a Tokai Hit thermochamber.

For the FRAP experiment, GFP fluorescence intensity has been measured in the bleached ROI. The GFP-fluorescence has also been measured in a control ROI (ROI_c) in the anterior compartment adjacent to the source. ROI_c has been chosen of identical dimensions to the ROI and the GFP fluorescence in this region has not been photobleached for FRAP and is therefore not expected to change. Experiments during which the GFP fluorescence in ROI_{cl} changed (increased or decreased) by more than 15% have been discarded. Similar to the nanobody

uptake assay, as a quality control, we have measured the gradient of eGFP-Dpp^{LOP} in order to confirm that its decay length is consistent with its posterior width, ℓ.

Within the bleached ROI, during recovery, a small proximo-distal gradient is expected (Extended Data Figure 4f). The spatial differences within the ROI are however too small to be detected considering the inherent noise in the FRAP data.

GFP fluorescence intensity measured in the bleached ROI as a function of time is used to plot the FRAP recovery curves. The average FRAP recovery curves (Extended Data Fig. 4b, number of individual FRAP experiments are $n = 9$ for large discs, $n = 6$ for small discs and n=6 for *pent*^{2} mutant discs) are used for the parameter determination by the Approximate Bayesian Computation method (see chapter 2.5.2 below).

We confirmed that the sample sizes in our data set for the FRAP assay are sufficient for accurate parameterization of transport parameters. We studied how the effective diffusivity and goodness of the fit (R^2) stabilizes as we increase the number of individual recovery curves considered for the average FRAP trace (Extended Data Fig. 4c,d). To determine the effective diffusivity D_{eff} from the average FRAP trace, we fitted a single dynamic equation[4]. As the number of recovery curves considered increase, the coefficient of determination R^2 fluctuates first until it stabilizes around a high value ($R^2 > 0.9998$; Extended Data Fig. 4c). In our analysis, we considered $n = 9$ for large ($\ell = 144\ \mu m$) discs, $n = 6$ for small ($\ell = 80\ \mu m$) discs and $n = 6$ for *pent*^{2} discs, well above the sample sizes at which the R^2 value stabilizes in the different conditions (7, 4 and 4, respectively). A similar analysis for D_{eff} (Extended Data Fig. 4d) yields the same conclusion (sample sizes for D_{eff} stabilization 6,4 and 3 recovery curves, respectively).

More than 50% of the GFP-Dpp fluorescence recovers within 90 minutes. It was previously shown that the remaining 50% recovers in a time scale which is much longer than these 90 minutes [4,8]. The long-term recovery reveals the existence of an immobile fraction, whose dynamics is captured in the long-term FRAP assay (see below) in which gradient formation is studied in longer time scales.

2.5.2 Procedure of parameter determination (Approximate Bayesian Computation)

In this section we illustrate the procedure for parameter determination for large, late third instar discs of posterior length $\ell = 144\mu m$ as an example. We first use the nanobody internalization assay to determine confidence intervals for k_N, k_r and k_o (chapter 2.2). This

is done by simultaneously fitting 13 experimental curves of nanobody accumulation to the theoretical uptake dynamics (Extended Data Fig. 3k). We thus estimate k_N, k_r and k_o together with their ranges of uncertainty (Fig. 2f). We find that, in large discs, eGFP-Dpp^{LOP} is internalized at a rate k_N within the range $(0.012 - 0.014)s^{-1}$. The time scale of internalization is therefore about $75s$, consistent with the reported $60s$ required to form a vesicle by endocytosis and $100s$ for Transferrin internalization in cultured cells[10-12]. The recycling rate k_r is estimated in the range $(1.7\text{-}1.8) \cdot 10^{-3}$s-1, corresponding to an average time scale of 10 minutes for recycling. This is in the range of reported recycling rates for the EGF ligand in culture cells[13,14]. The output rate k_o is in the range $(1.3\text{-}2.4) \cdot 10^{-4}s^{-1}$, a time scale of approximately one and half hours, also consistent with reported degradation rates of other ligands[15,16]. The experimental data and Wolfram Mathematica scripts used to perform these fits can be found here: https://github.com/zenah12/DppTrafficking- under the Nanobody_fits folder.

The remaining unknown parameters are k_{on}, k_{off}, k_i, D_0 and k_2. These parameters are constrained by i) the experimental FRAP data, ii) the experimental determination of the decay length λ in steady state which is the same as the decay length of the mobile fraction (Extended Data Fig. 2r,s and chapter 2.10), iii) the experimental determination of the extracellular fraction ρ and iv) the long-term FRAP assay to determine k_2. We first use the expression of the decay length, λ, given in Eq. (1) and the measured value for λ to solve for D_0 as a function of k_{on} and k_{off} (the remaining parameters in Eq. (1) are given by the nanobody assays). In our algorithm, we sample values of λ that are within the experimentally determined narrow range of $(27\text{-}29)\mu m$ for large discs (Extended Data Fig. 3e). This allows us to eliminate D_0 from the list of unknowns and leaves us with four unknown parameters k_{on}, k_{off}, k_i and k_2. To narrow the range of values for these four parameters, we considered a large number $(3 \cdot 10^7)$ of randomly chosen sets of parameter values (Extended Data Fig. 4j). We choose the prior ranges for these parameters in our sampling algorithm as follows.

For k_2 and k_{i}, random values were chosen in an interval defined by the long-term FRAP assay (10 hours; consistent with Entchev *et al.*[8]) and k_o (1.4 hours; from the nanobody assay, see above). More specifically, the long FRAP assay provides a lower limit for k_2 and k_{i}, and k_o provides an upper limit for k_{i} since $k_o = k_i + k_1$, and an upper limit for k_2 since the presence of the immobile fraction indicates that k_2 must be substantially smaller than k_o (i.e.

degradation in the mobile pool is faster than degradation in the immobile pool by definition). We therefore sampled k_2 and k_i in the interval [10^{-5}, 3 10^{-5}]s^{-1}. Finally, we did not make any *a priori* assumptions about the values of k_{on} and k_{off}. Instead, for these parameters, we chose random values within broad specified ranges spanning over 6 orders of magnitude (in the interval [10^{-5}, 1]s^{-1}; see Extended Data Fig. 4j). *A posteriori*, our assays did constrain these values within an order of magnitude (see below).

For each set of values sampled in the ranges described above, we calculated the expected relaxation in the FRAP experiment by numerically solving the dynamic equations for the five pools of Dpp under the conditions of the FRAP experiment (equations S1.1 to S1.5, with the assumption of bleaching a ROI near the source once steady state is achieved). We then compared the numerical solutions to FRAP for each unique parameter set to the experimental relaxation measured in the FRAP assay (Extended Data Figure 4a). This gave us a measure of the quality of the fit of each parameter set to the experimental data, that we quantified using the R^2. In this way, our analysis yields an R^2 value coupled with each of the $(3 \cdot 10^7)$ parameter sets considered. The C/C++ scripts used to perform the parameter sampling and obtain the numerical solutions to FRAP can be found here: https://github.com/zenah12/DppTrafficking- under the FRAP_numerics_ABC folder.

To obtain a posterior distribution for the remaining unknown parameters, we eliminate parameter sets that do not fit the data by setting a lower threshold to the value of R^2 that constitutes an acceptable fit (chapter 3.7), which provides a posterior distribution in the parameter space. Extended Data Figure 4j shows those sets of values with $R^2 > 0.92$ in the k_{on}, k_{off} plane. In these sets, the calculated recovery curves fit the data (see Extended Data Fig. 3m, for an example). This procedure determines which parameter values are consistent with the experimental FRAP data, the nanobody data, the decay length at steady state and the long-term FRAP assay (Extended Data Figure 4k).

This procedure reveals two distinct, non-overlapping clusters of parameter sets that can account for the experimental FRAP data, the nanobody data, the decay length at steady state and the long-term FRAP assay: one is characterized by small values of k_{on} and k_{off} (“lower cloud"), while the other is characterized by larger values ("upper cloud”) (Extended Data Fig. 4j). For the lower cloud, the extracellular fraction calculated from the dynamic equations (Eq. S2.23) is incompatible with the results obtained in the extracellular fraction assay. For large

discs, the extracellular fraction was estimated experimentally to be $\rho = 0.13 \pm 0.05$ (Fig. 2g). We therefore excluded all sets of parameter values for which the calculated extracellular fraction is outside the range of ρ values determined experimentally. For the set of parameter values in the lower cloud, the calculated values of the extracellular fraction ($\rho > 0.25$) significantly exceed the measure ones (Extended Data Fig. 4j). The remaining sets of values (the upper cloud, with $\rho < 0.10$) are shown in Extended Data Fig. 4k. The Wolfram Mathematica scripts used to analyze simulated data and impose restrictions on the value of $R^2$and ρ can be found here: https://github.com/zenah12/DppTrafficking- under the Posteriors_from_FRAP_and_rho folder.

Ultimately, from the ($3 \cdot 10^7$) sampled parameter sets, we find 58 (control), 74 (small discs) and 146 (*pentagone* mutants) sets that satisfied all five of our assays i) The nanobody assay ii) the FRAP data, iii) the experimental determination of the decay length λ in steady state and vi) the experimental determination of the extracellular fraction ρ and v) the long-term FRAP assay. These values define posterior distributions in a high dimensional plane which we visualize by plotting distributions for pairs of parameters as shown in Extended Data Fig. 4l.

For a discussion of the robustness of parameter determination to the chosen R^2 threshold and the value of ρ, see below (chapter 3.7).

Finally, the spatial pattern of the distributions projected on the different planes can in principle be understood *a posteriori* using the mode structure and expression for ρ that underlies the dynamical equations describing Dpp trafficking. The pertinent model structure is outlined in Section 1 and reference[1].

2.6 sfGFP-mKate2-Dpp (DppTimer) assay

2.6.1 Theory of the DppTimer assay

This assay is based on a fusion of Dpp with two fluorescent proteins: superfolder GFP (sfGFP; green), which matures the fluorophore in 5 minutes, and mKate2 (red), which matures in 20 minutes [17]. This implies that young molecules are only green, while older molecules are both green and red.

Here we therefore extend our five-compartment theoretical framework defined by Equations (S1.1)-(S1.5) in the document attached to Section 1 to describe the dynamics of Timer molecules. The maturation rate of sfGFP is fast (here considered instantaneous for simplicity)

whereas the mKate2 has a maturation rate of $\mu = 0.0006\mathrm{s}^{-1}$. We denote the concentration of the different pools of green molecules by gL_n, $\mathrm{gS}_\mathrm{n}^{(\mathrm{r})}$, $\mathrm{gS}_\mathrm{n}^{(\mathrm{l})}$, $\mathrm{gS}_\mathrm{n}^{(\mathrm{e})}$ and $\mathrm{gS}_\mathrm{n}^{(\mathrm{i})}$, of molecules that are green but not red by uL_n, $\mathrm{uS}_\mathrm{n}^{(\mathrm{r})}$, $\mathrm{uS}_\mathrm{n}^{(\mathrm{l})}$, $\mathrm{uS}_\mathrm{n}^{(\mathrm{e})}$ and $\mathrm{uS}_\mathrm{n}^{(\mathrm{i})}$ and red molecules by rL_n, $\mathrm{rS}_\mathrm{n}^{(\mathrm{r})}$, $\mathrm{rS}_\mathrm{n}^{(\mathrm{l})}$, $\mathrm{rS}_\mathrm{n}^{(\mathrm{e})}$ and $\mathrm{rS}_\mathrm{n}^{(\mathrm{i})}$. Following the five-compartment theoretical framework, we write down the following dynamic equations for the different pools of the green fluorescent, red fluorescent, and non-red molecules:

$$\frac{dgL_n}{dt} = \frac{D_0}{a^2}(gL_{n-1} - 2gL_n + gL_{n+1}) + k_{off}\left(gS_n^{(r)} + gS_{n+1}^{(l)}\right) - k_{on}gL_n + \frac{1}{2}(\nu_n + \nu_{n+1}) \quad \text{(S2.31)}$$

$$\frac{dgS_n^{(r)}}{dt} = -\left(k_{off} + k\right)gS_n^{(r)} + \frac{k_{on}}{2}gL_n + \frac{k_r}{2}gS_n^{(e)} \quad \text{(S2.32)}$$

$$\frac{dgS_n^{(l)}}{dt} = -\left(k_{off} + k\right)gS_n^{(l)} + \frac{k_{on}}{2}gL_{n-1} + \frac{k_r}{2}gS_n^{(e)} \quad \text{(S2.33)}$$

$$\frac{dgS_n^{(e)}}{dt} = k\left(gS_n^{(l)} + gS_n^{(r)}\right) - (k_r + k_i + k_1)gS_n^{(e)} \quad \text{(S2.34)}$$

$$\frac{dgS_n^{(i)}}{dt} = k_i gS_n^{(e)} - k_1 gS_n^{(i)} \quad \text{(S2.35)}$$

$$\frac{duL_n}{dt} = \frac{D_0}{a^2}(uL_{n-1} - 2uL_n + uL_{n+1}) + k_{off}\left(uS_n^{(r)} + uS_{n+1}^{(l)}\right) - k_{on}uL_n + \frac{1}{2}(\nu_n + \nu_{n+1}) - \mu\, uL_n \quad \text{(S2.36)}$$

$$\frac{duS_n^{(r)}}{dt} = -\left(k_{off} + k\right)uS_n^{(r)} + \frac{k_{on}}{2}uL_n + \frac{k_r}{2}uS_n^{(e)} - \mu\, uS_n^{(r)} \quad \text{(S2.37)}$$

$$\frac{duS_n^{(l)}}{dt} = -\left(k_{off} + k\right)uS_n^{(l)} + \frac{k_{on}}{2}uL_{n-1} + \frac{k_r}{2}uS_n^{(e)} - \mu\, uS_n^{(l)} \quad \text{(S2.38)}$$

$$\frac{duS_n^{(e)}}{dt} = k\left(uS_n^{(l)} + uS_n^{(r)}\right) - (k_r + k_i + k_1)uS_n^{(e)} - \mu\, uS_n^{(e)} \quad \text{(S2.39)}$$

$$\frac{duS_n^{(i)}}{dt} = k_i uS_n^{(e)} - k_1 uS_n^{(i)} - \mu\, uS_n^{(i)} \quad \text{(S2.40)}$$

$$\frac{drL_n}{dt} = \frac{D_0}{a^2}(rL_{n-1} - 2rL_n + rL_{n+1}) + k_{off}\left(rS_n^{(r)} + rS_{n+1}^{(l)}\right) - k_{on}rL_n + \mu\, uL_n \quad \text{(S2.41)}$$

$$\frac{drS_n^{(r)}}{dt} = -\left(k_{off} + k\right)rS_n^{(r)} + \frac{k_{on}}{2}rL_n + \frac{k_r}{2}rS_n^{(e)} + \mu\, uS_n^{(r)} \quad \text{(S2.42)}$$

$$\frac{drS_n^{(l)}}{dt} = -\left(k_{off} + k\right)rS_n^{(l)} + \frac{k_{on}}{2}rL_{n-1} + \frac{k_r}{2}rS_n^{(e)} + \mu\, uS_n^{(l)} \quad \text{(S2.43)}$$

$$\frac{drS_n^{(e)}}{dt} = k\left(rS_n^{(l)} + rS_n^{(r)}\right) - (k_r + k_i + k_1)rS_n^{(e)} + \mu\, uS_n^{(e)} \quad \text{(S2.44)}$$

$$\frac{drS_n^{(i)}}{dt} = k_i rS_n^{(e)} - k_1 rS_n^{(i)} - \mu\, rS_n^{(i)} \quad \text{(S2.45)}$$

Where $\mu = 0.0006s^{-1}$ is the maturation rate for the mKate2.

We solve equations (S2.31) – (S2.45) numerically to obtain estimates for the extracellular fraction of green and red molecules. We used these estimates to compute the age ratio (Fig. 4o). This age ratio (A^r) is defined as the fraction of red molecules in the extracellular *versus* intracellular pools and can be written as

$$A^r = \frac{R_{\text{ext}}/G_{\text{ext}}}{R_{\text{int}}/G_{\text{int}}} \quad \text{(S2.46)}$$

where G_{ext} and R_{ext}, the average sfGFP and mKate2 fluorescence associated to Dpp in the extracellular (bound and unbound) pools, whereas G_{int} and R_{int}, the average sfGFP and mKate2 fluorescence associated to Dpp in the intracellular pools.

The fraction A^r reveals whether the extracellular pool is enriched in "young molecules" (less red) compared to the total pool. In an Extracellular Diffusion (ExD) regime, intracellular molecules do not return to the extracellular pool. Because we find that the time scales of binding (few seconds) and endocytosis (tens of seconds) is much shorter than the time scale of mKate2 maturation (20 minutes), extracellular molecules are expected to be younger (fewer are red) than intracellular molecules in an ExD regime (Fig. 4o). Age ratio of 1 in both extracellular and intracellular pools thus indicates a high level of exchange between the extracellular and the intracellular pools: the age of molecules is the same intracellularly and extracellulary. Age ratio of 0 indicates that the two pools do not exchange: extracellular molecules are younger (fewer are red) than intracellular molecules.

2.6.2 Experimental procedure and quantification

Discs expressing Dpp$^{\text{Timer}}$ were mounted on a fluorodish in a fibrinogen clot and incubated with Cascade Blue conjugated dextran (Thermofisher Scientific, 3 000 MW) in order to label the outline of cells. Imaging was performed shortly after incubation, before Cascade Blue conjugated dextran can be internalized, and therefore the dextran signal serves to delimite the intercellular space. In living discs, GFP, mKate2 and Cascade blue fluorescence was imaged. For every image, three single confocal planes have been chosen to determine the age ratio. Cascade blue fluorescence has been processed by the Tissue Analyser plugin for

ImageJ[18] and used to define the mask of the outline of cells (Fig. 4j,k). The thickness of cell interfaces has been chosen according to the Abbe diffraction limit for our imaging setup of mKate2 and sfGFP. The average sfGFP (G_{ext}) and mKate2 (R_{ext}) fluorescence within the mask corresponds to the average Dpp concentration in the extracellular (bound and unbound) pools, whereas the average sfGFP (G_{int}) and mKate2 (R_{int}) fluorescence outside the mask corresponds to the average Dpp concentration in the intracellular pools (Fig. 4l-n). To determine G_{ext}, R_{ext}, G_{int} and R_{int}, corresponding background has been subtracted. Background has been measured at the edge of the corresponding gradients ($G_{ext}(x)$, $R_{ext}(x)$, $G_{int}(x)$ and $R_{int}(x)$). This average fluorescence has been then normalized by the area of the ROI used for the measurement. Age ratio (A^r) is defined as the fraction of red molecules in the extracellular *versus* intracellular pools (equation (S2.46)).

Age ratio of 1 indicates a high level of exchange: the age of molecules is the same intracellularly and extracellularly. Age ratio of 0 indicates that the two pools do not exchange: extracellular molecules are younger (less red) than intracellular molecules. In the bar plot in Fig. 4o, the experimentally determined age ratio is represented alongside theoretical age ratios for comparison. For ExD, Tr and P, age ratios have been calculated numerically using a modified version of the theoretical framework that accounts for the differential maturation times of the green and red fluorescent molecules; calculations were performed using the set of values in Fig. 3a.

2.6.3 Controls

Functionality. The functionality of Dpp fused to sfGFP and mKate2 in tandem has been tested by rescuing the *dpp* mutant phenotype of dpp^{d8}/dpp^{d12} flies by expressing UAS-sfGFP-mKate2-Dpp with the dppGal4 driver (Extended Data Fig. 6a).

Calibration of sfGFP and mKate2 fluorescent signal. If the Timer is efficient in conveying the information on the relative age of Dpp molecules, then "younger" Dpp molecules are expected to be detected closer to the source (*i.e.* the relative level of red mature mKate2 signal is lower), whereas further away from the source, most mKate2 molecules are matured (old). In order to compare the numbers of total (sfGFP) *versus* old Dpp molecules (mature mKate2) at different distances from the source, we calibrated the sfGFP fluorescent signal and the mKate2 fluorescent signal to each other.

The measured red and green fluorescence intensity (G, R) can be expressed as a function of the number of fluorescent molecules of each fluorophore (g, r) and a factor (f_g, f_r), which incorporates the properties of the corresponding fluorophores and the imaging conditions used:

$$G = f_g g \qquad \text{(S2.47)}$$

$$R = f_r r \qquad \text{(S2.48)}$$

We define F as

$$F = \frac{f_r}{f_g} \qquad \text{(S2.49)}$$

To measure F experimentally, we used GFP-trap beads (Chromotek) coated with fully matured sfGFP-mKate2 (purified by Emmanuel Derivery, see[7] for detailed protocol). For the coating, beads were washed with PBS 3 times and incubated in a solution containing the purified sfGFP-mKate2 for 2 minutes and subsequently washed x3 with and suspended in PBS. 10 µl of the solution has been pipetted on a coverslip. Once the beads were all sedimented on the coverslip, they were imaged on an inverted Leica TCS SP5 microscope using the conditions optimized for the imaging of sfGFP-mKate2-Dpp. As the number of molecules of the imaged sfGFP and mKate2 is the same in this condition (*i.e.* $g = r$, since both fluorophores are fully matured), the fluorescence intensity of each pixel using the sfGFP and mKate2 imaging conditions should be proportional to each other with the proportionality factor F:

$$\frac{R}{G} = \frac{f_r r}{f_g g} = \frac{f_r}{f_g} = F \qquad \text{(S2.50)}$$

Therefore we can determine $F = 1.08 \pm 0.03$ by plotting the sfGFP and mKate2 pixel intensities against each other and getting the corresponding proportionality factor (Extended Data Fig. 6b). It is worth disclaiming that F does not capture potential differences in the fluorescence behaviour (*e.g.* scattering) between sfGFP and mKate2 in the wing tissue and therefore is only an approximation to have an idea of the real concentration of fluorescent molecules in our system.

This way, the adjusted fluorescence intensity profiles for sfGFP ($g^*(x)$) and mKate2 ($r^*(x)$) (Extended Data Fig. 6d), which are proportional to the respective concentration profiles can be written as

$$g^*(x) = G(x) \qquad \text{(S2.51)}$$

$$r^*(x) = 1/\mathrm{F} \times R(x) \qquad \text{(S2.52)}$$

The ratio between the $r^*(x)$and $g^*(x)$ profiles is indicative of the relative age $A(x)$ of Dpp molecules as a function of position in the gradient. Note that closer to the source, there are less mature mKate2 molecules, confirming that Dpp molecules are younger. The relative amounts of sfGFP and mature mKate2 converge as we move away from the source, consistent with an increase in $A(x)$ with the distance to the source (Extended Data Fig. 6d-f). The value of F does not impact the spatial profile of $A(x)$.

Effect of pH on the Timer. It is well known that pH affects the fluorescence signal of certain fluorescent proteins. In the estimation of the age ratio of Dpp molecules extra- and intracellularly using the Dpp^{Timer}, a precise estimation of the ratio of sfGFP and mKate2 fluorescence is essential (see chapter 2.6 for the description of the assay). Indeed, a large portion of Dpp is in endosomal compartments inside cells, where pH is lower than 7. Acidic pH could in principle affect to a different extent the fluorescence of the two different fluorophores of the Timer molecule: sfGFP and mKate2.

In order to address this issue, we have performed the following experiments:

1) *In vivo*, we estimated the effect of pH on fluorescence of the sfGFP and mKate2 in the Dpp^{Timer} molecule in wing imaginal discs. We did this by neutralizing the pH to 7 in the endosomal compartments by means of bafilomycin treatment at 75 nM in Clone 8 medium for 30 minutes (Extended Data Figure 6h,i) and compared the fluorescence intensity of the two fluorophores before and after neutralizing the pH. To confirm the efficiency of bafilomycin in our treatment, we followed in vivo the pH of endosomes with LysoSensor™ (ThermoFischer Scientific): before bafilomycin treatment, discs were incubated in a solution of 1µM of LysoSensor™ in Clone 8 medium for 30 minutes. Acidotropic LysoSensor™ accumulated in acidic intracellular compartments (Extended Data Figure 6g). Following neutralization of pH upon bafilomycin treatment, LysoSensor™ fluorescence was decreased and diffused into the cytoplasm and the membrane of cells (no more accumulation in intracellular compartments can be observed, Extended Data 6g).
2) *In vitro*, we estimated the effect of pH on sfGFP and mKate2 fluorescence intensity using a purified Timer molecule bound to GBP-coated beads in buffer solutions (20 mM Hepes, 150 mM NaCl, pH7.7, 2.5% glycerol, 1mM DTT) at different pH (Extended Data Figure 6j);

In vivo experiments (#1) show that the effect of pH on Dpp-containing endosomes is similar for both fluorophores: at the acidic pH, fluorescence intensity decays by $62 \pm 4\%$ and $59 \pm 7\,\%$ for sfGFP and mKate2, respectively (Extended Data Figure 6h,i). Because both fluorophores are affected in parallel and the age measurement with the Timer is based on the ratio of their fluorescence, this result indicates that the acidic pH of the endosomes does not compromise the validity of the Timer.

Indeed according to the literature[19,20], the pKa of sfGFP and mKate2 are very similar, 5.9 and 5.4, respectively. At pH=pKa half the molecules are protonated and it is known that protonation of these fluorophores quenches the fluorescence *i.e.* at pH=pKa half of the fluorescence is expected to be lost. The observed decrease in fluorescence upon neutralization *in vivo* corresponds therefore to an average pH of 5.3-6 in Dpp-containing intracellular compartments, which is within the reported range of pH from early (6.2) to late (5.0) endosomes[21]. Consistently, our *in vitro* experiments (#2) confirm that, within this interval (5.0-7), the change of fluorescence intensity of sfGFP and mKate2 with pH is also similar. Note, that pKa values in cellular environments will differ from the values reported in the literature, hence we can only approximate the average pH in Dpp-containing intracellular compartments.

2.7 Internalized FRAP (iFRAP) assay

2.7.1 Experimental procedure

iFRAP experiments have been performed on discs expressing eGFP-Dpp (Fig.4c-f). Discs were mounted on a fluorodish in a fibrinogen clot. The imaging and photobleaching were performed on a SP8 microscope.

Mounted live discs were incubated on ice in a GBP-Alexa555 solution (0.003 µM) for 50 minutes. The dish with discs was then transferred to 25°C for 35 minutes. The temperature has been maintained by a Tokai Hit thermochamber on the SP8 confocal microscope and the signal of the internalized GBP-Alexa555 has been monitored. Discs were then washed with ice-cold clone 8 with its pH dropped to 3 by HCl in order to unbind eGFP-Dpp from the nanobody in the extracellular space (2 washes of 5 seconds each). In order to eliminate all stripped membrane-bound proteins, discs were then washed with large volumes (1 mL) of ice-cold clone 8 at physiological pH (3 washes of 15 minutes overall). A first image post-acid stripping and pre-bleaching has been taken. Alexa555 fluorescence in a ROI with dimensions

100 µm x 10 µm has then been photobleached. The rectangular ROI is perpendicular to the Dpp source, straddling the source into the posterior compartment. Alexa555 fluorescence is imaged every 5 minutes for 2 hours.

We observed an increase of Alexa555 fluorescence in the photobleached ROI. In order to confirm that the observed recovery of fluorescence comes from the internalized GBP-Alexa555 bound to eGFP-DPP and not from GBP-Alexa555 from the extracellular space that has potentially not been efficiently removed by acid wash, we have performed the following control experiments: (i) the efficiency of the acid stripping procedure has been tested to remove surface bound GBP-Alexa555 molecules by immunoblotting GFP bound to agarose GBP-coupled beads (GFP-trap) and GFP dissociated from GFP-trap beads following treatment of GFP-bound beads with an acid stripping solution (Extended Data Fig. 1j) and (ii) mounted live discs were incubated on ice in a GBP-Alexa555 solution for 50 minutes to label extracellular eGFP-Dpp, as above. Labelled extracellular eGFP-Dpp has then been stripped off by the acid wash protocol. Alexa555 fluorescence has then been monitored (Extended Data Fig. 5g,h): we did not observe any increase of Alexa555 fluorescence, confirming that our acid wash protocol efficiently removed all extracellularly bound GBP-Alexa555.

2.7.2 Theory for iFRAP experiment

We used the theoretical framework introduced in Section 1 to obtain numerical solutions for the iFRAP experiment for our full estimated parameter values in discs with $\ell = 144\mu m$ and $\ell = 80\mu m$. To do this, we had to implement the following modifications to the original equations (S1.1) – (S1.5) in in the document attached to Section 1:

- We consider a second population of molecules that are labelled with the nanobody and follow the labelled and unlabeled pool dynamics.
- When the nanobody is added, the concentration of the unlabeled extracellular pools (bound and unbound) becomes zero and the concentration of the labelled extracellular pools takes the steady state value of the corresponding unlabeled pools.
- We follow the labelled and unlabeled pool dynamics for 30 minutes. For these simulations we assume that:
    - The nanobody does not degrade with in the timescale of the experiment.
    - Unlabelled molecules that return to the extracellular space and newly produced molecules become immediately bound to the nanobody.

- Following 30 minutes of nanobody incubation the nanobody is washed. This means that the concentration of all extracellular pools (unbound and bound) is set to zero and that newly produced Dpp molecules are no longer labelled.
- We FRAP a ROI of ~12µm near the Dpp source to a bleaching depth of 0.1 and follow the recovery of the total nanobody concentration normalized to the prebleach (and post wash) concentration.

The theoretical values reported for the $\ell = 144\mu m$ and $\ell = 80\mu m$ were taken at $t = 2000s$ after bleaching and compared to the experimentally determined values (Fig. 4g, Extended Data Fig. 5i).

2.8 Photoconversion assay

2.8.1 Experimental procedure

Discs expressing eGFP-Dpp were mounted on a fluorodish in a fibrinogen clot and were incubated with GBP-Dendra2 solution (5 µg/ml in clone 8 pH 7.2) for 45 minutes at 25°C to allow extracellular and endosomal accumulation of eGFP-Dpp bound to GBP-Dendra2. Then, discs were acid washed 3 times with clone 8 pH 2.5 in order to unbind the nanobody from Dpp at the extracellular space. Subsequently, discs were washed 3 times with large volumes of clone 8 pH 7.2 and the dish was transferred to the stage of a Leica TCS SP8 microscope. After this, only endosomal nanobody molecules remain in the tissue: there is no signal in the extracellular space. In order to confirm that extracellular molecules have been removed efficiently by the acid wash and do not contribute to the subsequent accumulation of internalized Dendra2* signal (Dendra2*, denotes Dendra2 molecules which have been photoconverted to red), we incubated live discs on ice in a GBP-Dendra2 solution for 50 minutes to label extracellular eGFP-Dpp, as above. Labelled extracellular eGFP-Dpp has then been stripped off by the acid wash protocol. Subsequently, discs were transferred to 25^0C for 40 min to allow internalization of membrane bound GBP-Dendra2, Dendra2 was photoconverted in the anterior compartment and Dendra2* fluorescence was imaged (Extended Data Fig. 1a,b): we did not observe any intracellular accumulation of Dendra2* fluorescence 40 minutes after photoconversion, confirming that our acid wash protocol efficiently removed all extracellularly bound GBP-Dendra2*.

To study the behavior of GFP-Dpp bound to GBP-Dendra2, we studied the steady state decay length of GFP-Dpp^{LOP} without the nanobody in comparison to the recovered gradient of GBP-

Dendra2* bound to GFP-Dpp in the photoconversion experiment. For both conditions we have compared the values of $\phi = \lambda/\ell$ of eGFP-Dpp^{Gal4} gradient profiles and photoconverted Dendra2* gradient profiles (Extended Data Figure 1c). We confirmed that the values of ϕ were similar, indicating that the trafficking properties of these molecules are the same to the extent that they can generate the same gradient properties (Extended Data Figure 1c).

Discs were imaged with a 63x 1.4 NA oil objective and GFP fluorescence was monitored with a low power (0.5%) 488 laser, to avoid photo-conversion of Dendra2. Upon detection of GFP signal, an image of the disc pouch was acquired using a 562 laserline (Figure 1a). This image corresponds to the signal of the base-line red Dendra2, prior to photo-conversion. Subsequently, a ROI of 100 x 180 µm encompassing the anterior compartment was excited with a 405 laser line (Figure 1a), to induce photo-conversion of Dendra2, and the fluorescence of red-shifted Dendra2 was imaged every 12.5 min for 100 min (Figure 1a-c). During imaging, temperature was maintained at 25°C by a Tokai Hit thermochamber. Alternalively, photoconversion was performed in a ROI 100 x 180 µm in the posterior compartment adjacent to the A/P boundary, thereby containing only target cells and not Dpp-producing cells (Figure 1b).

In the experiment where we photoconverted cells in the anterior compartment (Fig. 1a,c), we also measured the dynamics of the Dendra2* signal in a region at the source boundary (Extended Data Figure 1d). The measured dynamics fits well the theoretical dynamics considering the parameterized values for large discs.

2.9 Growth rate measurements

We estimate the disc growth rate in eGFP-Dpp^{LOP} expressing wing discs using a previously established method[2]. In brief, larvae were staged from 48h to 152h after egg laying and imaged to measure their size and posterior compartment length ℓ (Extended Data Fig. 2o). The dynamics of growth is captured by exponential growth ($R^2 = 0.9473$)

$$A(t) = A_0 exp\,(-\tau\, g(t)) \qquad \text{(S2.53)}$$

where A_0 is the asymptotic area and the growth rate $g(t)$ decays exponentially with time (here, age of discs after egg laying) according to the equation

$$g(t) = \frac{b}{\tau} exp(-t/\tau) \qquad \text{(S2.54)}$$

where b is a constant factor related to the maximum growth rate and τ is the decay time of the growth rate.

We fitted the observed disc area as a function of the age of discs after egg laying to equation (S2.53) to estimate the growth rate g as a function of the age of discs (see equation (S2.54)). In order to specifically estimate the growth rate for discs of posterior compartment length of $\ell = 144\ \mu\text{m}$ and $\ell = 80\ \mu\text{m}$, we need to first determine the age after egg laying corresponding to these sizes of discs. For that, we have established a correlation between disc area A and disc posterior length ℓ (Extended Data Figure 2p): there is a power-law relationship relating A and ℓ with the growth anisotropy $m = g_x/g = \frac{\dot{\ell}/\ell}{\dot{A}/A}$. Using m, the area of discs of $\ell = 144\ \mu m$ and $\ell = 80\ \mu m$ posterior length has been determined (Extended Data Figure 2p). Using this area and equation (S2.53), we estimated the age of discs of $\ell = 144\ \mu m$ and $\ell = 80\ \mu m$ posterior length and then, using equation (S2.54), the corresponding growth rates.

2.10 Measurement of the mobile fraction decay length

In order to measure the mobile fraction decay length, we exploit the observation from the long-term FRAP assay that the mobile pool relaxation is much faster than the relaxation of the immobile pool (30 minutes *versus* 10 hours, respectively). We bleached eGFP-Dpp in the entire posterior compartment of the disc and let the eGFP-Dpp molecules from the fast-relaxing mobile fraction recover for 30 minutes (Extended Data Fig. 2r). We then measured the recovered gradient profile (the profile of molecules corresponding predominantly to the mobile pool) in the posterior compartment and estimated its decay length (λ_M) by fitting to an exponential function. We then compared for each disc the decay length of the steady-state eGFP-Dpp gradient before bleaching (λ_T, corresponding to the total pool of molecules) with the decay length of the mobile pool (Extended Data Figure 2s). We found that $\lambda_T \simeq \lambda_M$. This shows that the fast-relaxing mobile pool quickly forms a gradient at the appropriate decay length (i.e. a decay length which scales with the size of the tissue). For quantitative implications of this observation and the discussion on the steady-state approximation of the gradient used in this report, see chapter 3.9).

2.11 Estimation of leakage from extracellular space in the disc epithelium

In order to estimate the loss of extracellular molecules by leakage, we have: i) generated a transgenic fly expressing sGFP^{Dpp}; ii) estimated the upper bound value of the leakage rate k_L^{max} and iii) performed chase experiments at 25°C and 4°C to evaluate the loss of sGFP^{Dpp} from the epithelium due to leakage.

2.11.1 sGFP^{Dpp}

In sGFP^{Dpp}, GFP is inserted into the Dpp coding sequence after the site of Furin cleavage in the Golgi, which separates the Dpp propeptide (with its own signal peptide) and the C-terminal rest of the protein. In this construct, we engineered a STOP codon at the GFP C-terminus so that the mature peptide is not translated (see scheme in Extended Data Figure 2d). Therefore, upon Furin cleavage of this chimeric protein, only GFP is produced without the C-terminal mature peptide which is not translated. This mature C-terminal fragment is the morphogen that generates a gradient. Using the Gal4 system, we express it by means of a Dpp enhancer region. Therefore, this molecule (which we term sGFP^{Dpp}) retains the 5'UTR of Dpp, the signal peptide of Dpp and the cleavage sites of Dpp followed by GFP: GFP mRNA is transcribed, and the protein, translated, cleaved and traffics like Dpp. Note that there is no receptor that retains GFP at the membrane of the epithelial target cells and that GFP is not endocytosed as it is only present in the extracellular space: in this system there is only extracellular diffusion and, potentially, leakage. We have therefore generated a simplified system to study a potential role of leakage using a GFP molecule which shares with Dpp all the features of production, trafficking and secretion characteristics of the producing cells.

Discs expressing sGFP^{Dpp} have been fixed, mounted and GFP fluorescence has been imaged as described in Methods. Note, that, unlike the reagent used in the study by Stapornwongkul et al.[22], GFP is robustly seen in the target tissue (Extended Data Figure 2e). To evaluate the apicobasal localization of sGFP^{Dpp} , cell cortex in fixed discs expressing sGFP^{Dpp} has been labelled by F-actin phalloidin (Methods). As confirmed by apical colocalization with phalloidin, most sGFP^{Dpp} is seen in a 1µm thick region within the epithelium in the apical side (Extended Data Figure 2e). It is worth noting that sGFP^{Dpp} is extracellular, as it does not appear in intracellular endosomal structures (Extended Data Figure 2e).

2.11.2 Estimation of the upper bound for the leakage rate k_L using sGFP^{Dpp}

In the target epithelium, this sGFP^{Dpp} does not form a gradient (see Extended Data Figure 2e,f). As discussed above, the only phenomena that describe sGFP^{Dpp} transport are diffusion D and leakage k_L. The decay length of Dpp λ would then be defined by these two parameters: $\lambda = \sqrt{D/k_L}$. A flat spatial profile therefore indicates that the actual levels of leakage and diffusion in the wing cannot generate a gradient by itself. We can consequently estimate an upper bound for the leakage rate k_L assuming a potential decay length of Dpp about 3 fold

the target tissue length L ($\lambda > 3L$) and considering the highest possible value of diffusion coefficient $D < 100\,\mu m^2/s$, the diffusion coefficient of a molecule of the size of Dpp in the aqueous environment of the extracellular space without a binding partner (see note below): $k_L < D/\lambda^2$, therefore $k_L < 0.0005\ s^{-1}$. These estimations are conservative since the diffusion of GFP in the extracellular space is likely to be lower than in the aqueous environment, and we observe no decay in the GFP profile suggesting that the GFP decay length is more than 3-fold larger than the target tissue size (see Extended Data Figure 2f).

Note that this upper bound for the leakage rate obtained in our measurements, is 150-fold smaller than the leakage rate $k_L = 0.075\ s^{-1}$ estimated in Stapornwongkul et al.[22] for their secreted GFP, indicating that sGFP^{Dpp} has different leakage properties (probably due to the place where it is secreted, see chapter 4.3.1), and in particular, that leakage is very small if at all existing in the Dpp morphogen system.

Note: we estimate the diffusivity of the size of Dpp in water using the Stokes-Einstein equation:

$$D = \frac{k_B T}{6\pi\mu R_0}$$

Where k_B is the Boltzman constant, T is the temperature, μ is viscosity and $R_0$is the solute radius. Using, $k_B = 1.4\ 10^{-23} J/K$, the viscocity of water $\mu = 10^{-3}$Psc s, the temperature of our experimental setting $T = 298.15\ K$ and considering the size of Dpp as $R_0 = 2.8\ 10^{-9}$m, we obtain an estimate for $D \approx 80\ \mu m^2 s^{-1}$.

2.11.3 Chase experiments using sGFP^{Dpp}

In order to independently evaluate whether the leakage rate of sGFP^{Dpp} is consistent with the upper bound for k_L estimated above, discs expressing sGFP^{Dpp} were cultured in Clone 8 medium *ex vivo* for 1 hour at 25°C. Discs were then fixed, mounted and GFP fluorescence has been imaged as described above (Methods).

The total GFP fluorescence has been estimated for each disc using the orthogonal view of the corresponding z-stacks in ImageJ. The estimated total GFP fluorescence was then compared to the total fluorescence of GFP in a control condition, where dissected sGFP^{Dpp}-expressing discs were immediately fixed without a chase of 1h (Extended Data Figure 2g,h).

In the study by Stapornwongkul et al.[22], the leakage rate is estimated to be 0.075 s^{-1}, corresponding to a time scale for the disappearance of molecules from the epithelium of 13

seconds. If this was true for sGFP^{Dpp}, then one would expect that sGFP^{Dpp} disappears from the epithelium in this 13 seconds. We could not detect any temporal decay in the signal, confirming that sGFP^{Dpp} does not leak in one hour time *i.e.* well beyond the 13 seconds expected for the estimation of the leakage rate in Stapornwongkul et al.[22] and the 33 minutes corresponding to the upper bound of the leakage rate $k_L = 0.0005\ s^{-1}$estimated above (chapter 2.11.2). This is indeed consistent with the fact that sGFP^{Dpp} does not form a gradient (Extended Data Figure 2e,f). We repeated this experiment at 4˚C, to exclude the influence of *de novo* production of sGFP^{Dpp} in this experiment (Extended Data Figure 2g,h).

2.11.4 Estimation of GFP-Dpp leakage from extracellular space in the disc epithelium

In order to estimate the loss of extracellular GFP-Dpp molecules by leakage, we labelled extracellular eGFP-Dpp in eGFP-Dpp^{LOP}-expressing discs with GBP-Alexa555 by an extracellular staining protocol (chapter 2.3.2). We then chased the living disc in Clone 8 for 7 hours at 4˚C (where no production, internalization or degradation happens) to determine how fast could Dpp molecules leak from the extracellular space (Extended Data Figure 2a,b). Discs were then fixed, mounted and GBP-Alexa555 fluorescence has been imaged as described above (Methods). The total GBP-Alexa555 fluorescence has been estimated for each disc in a ROI in the posterior compartment by fitting the corresponding profile of Alexa555 fluorescence to an exponential function and taking the product of the corresponding decay length and amplitude (note that $\int_{x=0}^{x=\infty} C_0 e^{-x/\lambda} = C_0\lambda$). The estimated total GBP-Alexa555 fluorescence was then compared to the total fluorescence of GBP-Alexa555 in a control condition (extracellular staining without a chase of 7h ; Extended Data Figure 2a). We show that the decay is negligible, consistent with a scenario in which leakage is not important in the Dpp system.

For more details on the potential loss of Dpp from the extracellular space see chapter 4.3 below. We have also considered theoretically the impact of leakage on our parameter determination (see chapter 3.10).

2.12 Requirement of recycling for gradient formation

In order to address the role of endocytic recycling in the formation of the Dpp gradient, we have silenced Dpp recycling in the posterior target cells by RNAi through expression of previously validated dsRNA[23,24] for the canonical recycling Rabs, Rab4 and Rab11. Silencing was applied for 4 days before dissection by using the Gal4 system controlled by Gal80^{ts} (Extended

Data Fig. 6k-n). In these conditions, the Dpp recycling rate k_r is significantly affected, as measured by the nanobody uptake assay (Extended Data Figure 6o). We observe a significant shortening of the decay length of the eGFP-Dpp^{LOP} gradient upon partial silencing of recycling by RNAi (Extended Data Fig. 6k-n). Moreover, measuring decay lengths of eGFP-Dpp^{LOP} gradients for discs of different sizes revealed a scaling phenotype upon silencing of Rab4: gradients do not expand as the disc grows (Extended Data Figure 6m). Taken together, this shows that Dpp recycling plays an important role in gradient formation and scaling.

3 SUPPLEMENTARY NOTES: Quantitative considerations

3.1 Different modules contributing to the steady-state decay length

We showed above (Section 1 and reference[1]) that the dynamic equations which capture five pools of Dpp lead to a steady-state decay length lambda with

$$\lambda^2 \approx \frac{D_0}{k_{on}} + \frac{D_0}{k_{on}}\frac{k_{off}}{k} + \frac{D_0}{k_{on}}\frac{k_{off}}{k}\frac{k_r}{k_i+k_1} + a^2\frac{k_r}{4(k_i+k_1)}\frac{k_{off}}{k_{off}+k} \qquad \text{(S2.55)}$$

This expression has four key terms, which correspond to different transport modules (Fig. 1e-f). The first term $\frac{D_0}{k_{on}}$ describes the "unbound module". It expresses the contribution to λ^2 of the unbound extracellular pool of molecules alone. This is the only transport module in a pure extracellular diffusion model as formulated before [9,25] and corresponds to a scenario where $k_{off} = 0$. If morphogen binding is reversible, $k_{off} \neq 0$, the other three terms come into play. The second term $\frac{D_0}{k_{on}}\frac{k_{off}}{k}$, the "bound module", also includes molecules bound to receptors which could in principle unbind with rate k_{off} and thereby contribute to the diffusing unbound pool. Internalization by endocytosis with rate k counteracts this process and eliminates the possibility of some of these bound molecules to be transferred to the unbound pool.

The third term, $\frac{D_0}{k_{on}}\frac{k_{off}}{k}\frac{k_r}{k_i+k_1}$, the "recycling module", includes a contribution of the endosomal pool. Molecules can be recycled back with rate k_r to the extracellular bound pool, which itself can then contribute to the diffusing unbound pool. Degradation at rate k_1 or immobilization at rate k_i eliminates the possibility that this endosomal pool contributes to the diffusing pool. If there is no recycling $k_r = 0$, this term vanishes and only unbinding and endocytosis remain relevant among the trafficking rates.

The first three terms, where the extracellular diffusivity D_0 is important, are independent of the cell size a. The fourth term, on the other hand, $a^2 \frac{k_r}{4(k_i+k_1)} \frac{k_{off}}{k_{off}+k}$ is independent of D_0. It describes a length scale that is exclusively due to the intracellular trafficking rates and the cell size a. This term describes the spreading of the morphogen by pure transcytosis: molecules move from one cell to the next by unbinding from one cell and binding to the adjacent neighbour cell with negligible diffusivity ("bucket brigade", [26]). The decay length is an increasing function of the cell size a, since that determines the distance a molecule can travel in a single step of transcytosis.

This term is enabled by recycling and unbinding, by which molecules from one cell are made accessible to the neighbouring cells. This process is counteracted by degradation/immobilization inside cells with rate $(k_i + k_1)$. This term is largest if $k \ll k_{off}$ and both k and k_{off} have to be non-zero. Note that, when $D_0 = 0$, only the fourth term contributes to gradient formation. This is the extreme transcytosis regime discussed in the main text and proposed by Wolpert [26].

The transcytosis term also shows how a non-zero decay length can occur in the absence of extracellular diffusion ($D_0 = 0$). This can be seen in our system of equations (see equations S1.1 to S1.5 in the document attached to Section 1): a Dpp molecule in the extracellular pool going from the bound to the unbound state on the right side of the cell n (from S_R^n to L_n) can go directly, without the participation of extracellular diffusion, to the extracellular pool bound on the left side of the cell $n+1$ (S_L^{n+1}). The justification for this idea is the small distance (in the order of 10 nm) between adjacent cells which are packed in a tight epithelium; in this scenario a molecule that is bound to a receptor on one cell can be passed to a receptor on the neighbouring cell.

For a particular set of values for the rate parameters that generate a specific decay length, λ, each of these four terms carries a relative weight. We use the relative weights of the four terms to define whether transport of Dpp is in a regime of extracellular diffusion, transcytosis or, in between, in a regime of combined transport (Fig. 1e,f). For all our experimental conditions, the parameter values indicate that the weights of the bound and transcytosis modules are small (Extended Data Fig. 8d).

3.2 Effect of k_i and k_2 on the decay length

The rate at which molecules move to the immobile fraction, k_i, and the degradation rate at the immobile fraction, k_2, have a negligible contribution to the morphogen decay length. Although k_i appears in the expression for λ, it always appears together with k_1 which is several orders of magnitude larger (see Equation S2.55). It follows that k_i has little effect on the decay length. The value k_2 determines the rate at which molecules degrade in the immobile fraction. Molecules in the immobile fraction do not return to any of the other pools and therefore they do not contribute to the spreading of molecules. Therefore, k_2 does not contribute to the decay length. We therefore did not consider these two parameters in Figure 3a and Extended Data Figures 4m and 1l.

3.3 Effective rates of Dpp transport

The morphogen gradient range (i.e. its decay length), depends on the effective diffusivity of the morphogen and its effective degradation rate as the molecules spread in the tissue[1,4,9].

These effective rates characterize the apparent diffusion and degradation of the total pool of morphogen molecules considered at the tissue length scale. The apparent diffusion and degradation depend only in part on the Brownian motion of molecules or their lysosomal degradation at the cellular length scale, and are also affected by other transport phenomena[1,4,9].

The effective diffusivity and effective degradation at the tissue level has been previously estimated by fitting the dynamics of FRAP recovery using a single dynamic equation[4]. With a single equation, one does not distinguish between the dynamics of the different pools, but instead describes the effective behavior of the total pool of Dpp molecules at the tissue level. Using this procedure, our FRAP data yields an effective diffusivity $D_{\text{eff}} \simeq 0.36 \pm 0.02\ \mu m^2 s^{-1}$ for large discs (Extended Data Fig. 4e, Extended Data Table 2). Interestingly, this effective diffusivity D_{eff} is three-fold smaller than the diffusivity D_0 of unbound Dpp molecules estimated above (Fig. 3a). The effective diffusivity and extracellular diffusivity are conceptually different, and this is confirmed here by our measurements.

3.4 Effective rates during scaling

During growth, the decay length of the gradients increases to stay proportional to the size of the organ (Fig. 2a). This gradient scaling must be mediated by changes in the transport rates.

It has previously been shown that Dpp gradient scaling in the fly wing is regulated through changes in the effective degradation rate of Dpp as a function of tissue size [2]. We confirm this finding in this report (Extended Data Fig. 4e).

3.5 Contribution of transport parameters to the decay length: Boost B_i (Extended Data Figure 5c-e)

Consider a gradient with a decay length given by equation (S2.55) introduced in chapter 2.1 and shown here again for convenience.

$$\lambda^2 \approx \frac{D_0}{k_{on}} + \frac{D_0}{k_{on}}\frac{k_{off}}{k} + \frac{D_0}{k_{on}}\frac{k_{off}}{k}\frac{k_r}{k_i+k_1} + a^2\frac{k_r}{4(k_i+k_1)}\frac{k_{off}}{k_{off}+k}$$

We quantify the contribution of a given transport parameter p_i to the decay length by introducing the boost B_i due to the presence of that parameter,

$$B_i = \frac{\lambda}{\lambda(p_i=0)} \qquad \text{(S2.56)}$$

where λ is the observed value of the steady-state decay length of the gradient (consistent with the parametrized set of values according to Equation S2.55), and $\lambda(p_i = 0)$ is the calculated decay length (according to Equation S2.55) using the parameterized values except that p_i is set to zero ($p_i = 0$).

In our quantification procedure, k, $k_o = k_i + k_1$ and k_r are already specified within narrow ranges by the nanobody uptake. The value of D_0 is also constrained by the measured value of the decay length λ (see chapter 2.5.2). It follows that, just using the nanobody internalization assay and the steady-state decay length, the only parameters that are unknown in the expression for B_i are k_{on} and k_{off}. We evaluate the expression for B_i around the average values of k, k_o, k_r and D_0 obtained using the nanobody assay and control decay length to obtain an expression for B_i that only depends on k_{on} and k_{off}. This allows us to plot the value of B_i as a contour plot *versus* k_{on} and k_{off} as shown in Extended Data Fig. 5c,d. Finally, note that the value of k_2 does not impact the decay length and so has no effect on the boost function. This is because k_2 simply specifies a degradation rate in the immobile pool that does not contribute to the spreading of morphogen molecules in the tissue.

We show that large discs are in a combined transport regime, where extracellular diffusivity, recycling and unbinding are all important for the formation of the gradient. Consistently, the boosts B_{k_r}, $B_{k_{\text{off}}}$ and B_{D_0} are high (Extended Data Figure 5e). Consistent with a large B_{k_r}, the decay length of the gradient is significantly shortened upon partial silencing of recycling by

RNAi through expression of dsRNA for the recycling Rabs (Rab4 and Rab11) in the posterior target cells (Extended Data Fig. 6k-n).

3.6 Ratio of the recycling and unbound modules (Figure 3d and Extended Data Fig. 7b)

The recycling and the unbound modules (λ_r^2 and λ_u^2 , respectively) (chapter 2.1.1, 3.1) are the key contributors to the decay length under the different experimental conditions considered in our analysis (see main text; the other two modules are negligible in all the experimental conditions studied in this report). To visualize the relative weight of these two terms in our parameterization, we plotted the contour plots of their ratio $R_{r,u} = \frac{\lambda_r^2}{\lambda_u^2}$ on the $(k_{off},\ k)$ plane alongside with the cluster of parameterized values for the three different experimental conditions ($\ell = 144$, $\ell = 80$ and *pent*[2], see Fig. 3d and Extended Data Fig. 7b).

The ratio $R_{r,u}$ reduces to the following expression,

$$R_{r,u} = \frac{k_{off}}{k}\left(\frac{k_r}{k_i+k_1}\right) \qquad \text{(S2.57)}$$

The values for k_r and $k_o = k_i + k_1$ were determined in narrow intervals by the nanobody assay. We used the estimated values for k_r and k_o to plot $R_{r,u}$ on the $(k_{off},\ k)$ plane as shown on Fig. 3d in the main text. Note that in the plot of Fig. 3d we used the mean values of k_r and k_o averaged over our three experimental conditions ($\ell = 144$, $\ell = 80$ and *pent*[2]). The values of k_r and k_o are comparable in these three conditions and, consistently, the plots using the individual estimates for each condition are very similar (Extended Data Fig. 7b) justifying the use of the averages in Fig. 3d.

3.7 Analysis of the robustness of parameter determination (Extended Data Figure 5a,b)

To investigate how constrained are our solutions, we first studied how the constraints imposed by the quality of the fit to the FRAP assay impacts the solution space and our conclusions. To address this, we varied the threshold imposed for R^2 in our fitting routine described above (chapter 2.5.2). The fits presented in our analysis for large discs (ℓ=144 µm posterior length) satisfied $R^2 > 0.92$. We looked at the "cloud" of solutions in the $(k_{on},\ k_{off})$ plane when $0.92 > R^2 > 0.90$ and $0.90 > R^2 > 0.86$. We found that allowing solutions with lower goodness of fit leads to a wider "cloud" of solutions. This however remains in the "combined transport regime", where recycling and receptor unbinding continue to provide a

significant boost for the decay length (Extended Data Fig. 5c-e). The cloud of solutions remains distinct from the cloud of solutions obtained in the small disc ($\ell = 80\ \mu m$ posterior length) and *pent*^{2} solutions which correspond to a regime of extracellular diffusion (Extended Data Fig. 5a). Solution in this Extracellular diffusion cloud only appear if R^2 is permitted to drop below 0.85. A similar analysis for small discs (ℓ=80 μm posterior length) and *pentagone* mutants are likewise robust to changes in R^2.

A similar analysis, where we relaxed the upper limit for the extracellular fraction ρ, also revealed that our control fits are robust to variations up to 245% in the value of ρ (Extended Data Fig. 5b): the solutions in the Extracellular diffusion cloud require $\rho_{\text{th}} > 0.27$ (*versus* the measured $\rho = 0.11$). Here ρ_{th} indicates the value of the extracellular fraction above which the theoretical FRAP recoveries fit the experimental data for small ($k_{on},\ k_{off}$) (i.e. the lower "cloud" found on the ($k_{on},\ k_{off}$) plane). A similar analysis in small and pentagone mutant discs indicates that our conclusions are robust to a 125% change in small discs and 165% change in *pentagone* mutant discs. These were well above the confidence intervals of our measured values for the extracellular fraction indicating that our conclusions are robust to fluctuations in these measurements.

3.8 Changes in λ with k_{on}, k_{off} and D_0 (Extended Data Figure 7a)

In this section we investigate whether changes in all three parameters k_{on}, k_{off} and D_0 can mediate continuous and monotonic changes in λ. To do this, we used the expression for λ in Equation S2.55 and searched for continuous and monotonic changes in k_{on}, k_{off} and D_0 that could lead from the observed values of k_{on}, k_{off} and D_0 in small discs to those in large discs while also changing the decay length from $\lambda \approx 15\mu$m to $\lambda \approx 27\mu$m monotonically. We found that this is possible and we show a plausible scenario with specific variations in k_{on}, k_{off} and D_0 that connects between small and large discs (Extended Data Fig. 7a).

3.9 Dpp gradient is in quasi steady-state

3.9.1 Discussion on the possible non-stationarity of the system

As discussed in SI 1.1, in order to obtain the expression for the Dpp gradient decay length (equation (S1.6)), the dynamic equations (S1.1) to (S1.5) are solved at steady-state. We then use this expression for the determination of the transport parameters. In this chapter we rationalize the use of this steady-state approximation.

A previous report by Fried and Iber[27], discussed a situation where growth by itself can extend a gradient with time. This effect occurs in a particular regime where the turnover of molecules is slow and comparable or slower than the rate of tissue growth. If the ligand molecules turn over faster than the growth rate, a quasi-steady state assumption holds and the gradient cannot be stretched by growth. If molecules turn over very slowly, they are carried in the growing tissue and the gradient can stretch via growth.

We have addressed the potential non-stationarity of our system by: 1) confirming that our system comprises two pools with distinct dynamics; 2) comparing the measured growth rates during development with the measured relaxation timescales of both mobile and immobile pools, 3) measuring the decay length of the mobile and immobile pools and 4) performing a theoretical analysis to discuss the effects of growth and non-stationarity on our system.

The long-term FRAP assay in both small and large discs (chapter 2.4) confirms that the turn-over of molecules occurs with different dynamics in two different pools: a fast mobile pool and a slow immobile pool (Extended Data Figure 2k-n). Indeed, the total recovery dynamics over 10 hours cannot be fitted by a single exponential, but fits a double exponential (Extended Data Fig. 2l,n). Therefore, we have to discuss both pools separately to address whether the steady state assumption is valid.

Fast pool. The fast pool relaxes in half an hour *i.e.* with a rate much faster than the growth rate in both early and late discs, where the size doubles in 20h and 25h, respectively (Extended Data Figure 2o,q). These growth rates were measured for the precise genetic conditions considered in this report (chapter 2.9, Extended Data Figure 2o,q).

We have then measured the decay lengths of the total pool gradient (λ_T), the mobile pool gradient (λ_M) and the immobile pool gradient (λ_I) using the procedure described in chapter 2.10. We first measured the decay length of the steady-state gradient before bleaching (λ_T), we bleached GFP-Dpp in the entire target area of the posterior compartment, and then we measured the decay length of the mobile pool (λ_M) after half an hour of recovery (Extended Data Fig. 2r). Note that, indeed, in half an hour the mobile pool has recovered close to completion, while the immobile pool has not recovered yet. We found that $\lambda_T \simeq \lambda_M$ (Extended Data Fig. 2s; since $\lambda_T \simeq \lambda_M$, then $\lambda_T \simeq \lambda_I$ too as expected; see chapter 3.9.2 below). This shows that the fast-relaxing mobile pool quickly forms a gradient with the appropriate decay length (i.e. a decay length which scales with the size of the tissue) and that

this gradient is in a quasi-steady state (recovery is much faster than growth). Thus, growth has no impact on the decay length of the mobile pool gradient. This validates our parameterization.

Indeed we have estimated the parameter values of Dpp transport based on the fast dynamics of the mobile pool which is in steady-state in a short time scale: 1) the fast dynamics of the nanobody internalization assay (30 minutes); 2) the fast dynamics of recovery of the mobile pool in FRAP; 3) the size of the extracellular pool, dominated by rates ($\mathrm{k_{on}}$, k_{off}, D_0, k) which are all much faster than the growth rate and 4) the decay length of the total pool (λ_T). As noted above, the total pool could in principle pose a problem, because it contains a fast and a slow component: the decay-length of the total pool may not have been itself in steady state. However, we show above that $\lambda_T \simeq \lambda_M$ and therefore the decay length of the total pool serves as a proxy for the decay length of the mobile pool.

In summary, our parameterization assays are based on the mobile pool, which is in steady-state. This validates our fitting routine to the assays, since the dynamics of the assays are much faster than growth. Our validated parameterization uncovers that the scaling of the mobile pool, which is in quasi steady-state, is mediated by changes of $\mathrm{k_{on}}$, k_{off} and D_0.

Slow pool. The gradient of the slow, immobile pool has to be discussed separately. The immobile pool relaxation is slower than the growth rate and is therefore not in steady-state. Note however that the immobile pool not being in steady state is incorporated in our model and this does not invalidate our steady state assumption for the mobile pool and the parameter estimates. For instance, when we performed the Approximate Bayesian Computation method to fit the FRAP data, and in other numerical estimations, we used the dynamic equations (equations S1.1 to S1.5); we did not make any steady-state assumption about the immobile pool, but instead consider the full dynamics.

In order to better understand the properties of the immobile pool and in particular why it scales with system size, we have developed theory that considers a slow and a fast pool in a growing tissue (see chapter 3.9.2 below).

3.9.2 Effect of growth on the Dpp gradient profile

In this chapter we consider the effects of growth and non-stationarity in our analysis. Our long-term FRAP experiments in both small and large discs reveal the existence of two pools

for which the fluorescence recovers differently, indicating that the turn-over of molecules occurs with different dynamics in two different pools: a fast mobile pool and a slow immobile pool. The mobile pool relaxes in the timescale of 30 minutes and is therefore at quasi-steady state in our experimental assays. This is not true for the immobile pool which relaxes in the timescale of 10 hours. The effective dynamics of the two pools in a growing domain are described by

$$\partial_t C + v_x \partial_x C + gC = D_{eff} \partial_x^2 C - k_{eff} C + s \qquad \text{(S2.58)}$$

$$\partial_t C_I + v_x \partial_x C_I + gC_I = \bar{k}_i \, C - k_2 C_I \qquad \text{(S2.59)}$$

where $C(x,t)$ and $C_I(x,t)$ are the concentration profiles of the mobile and immobile pools respectively, v_x is the local cell velocity, D_{eff} and k_{eff} are the diffusion coefficient and degradation rate of the mobile pool that are estimated by FRAP[4,28], $\bar{k}_i$ is the rate at which molecules move from the mobile to the immobile pool, k_2 is the degradation rate in the immobile pool and g is the growth rate defined by $g = \partial_x v_x (1+\epsilon)$, where epsilon is the tissue anisotropy defined by $\in = \partial_y v_y / \partial_x v_x$. s is a term capturing morphogen production in the source. Eq (S2.58) and (S2.59) in the scaled coordinate system are given by

$$\partial_t \tilde{C} = \frac{D_{eff}}{L^2} \partial_r^2 \tilde{C} - (k_{eff} + g)\tilde{C} + s(r) \qquad \text{(S2.60)}$$

$$\partial_t \widetilde{C_I} = \bar{k}_i \tilde{C} - (k_2 + g)\widetilde{C_I} \qquad \text{(S2.61)}$$

where $r = \frac{x}{L}$ and $\tilde{C}(r,t) = C(rL(t),t)$, $\tilde{C}_I(r,t) = C_I(rL(t),t)$. Let us now assume that the mobile pool scales so that $\tilde{C}(r,t) = \tilde{C}_0(t)\xi(r)$ with $\xi(r)$ being a scaling function which does not depend on the size of the tissue and captures the invariability of the gradient shape as the tissue grows. It follows that $\partial_t \tilde{C} = \frac{\dot{\tilde{C}}_0}{\tilde{C}_0}$ (see reference[2]) and equation (S2.60) can be written as

$$0 = \frac{D_{eff}}{L^2} \partial_r^2 \tilde{C} - (k_{eff} + g + \frac{\dot{C}_0}{C_0})\tilde{C} + s(r) \qquad \text{(S2.62)}$$

In the wing imaginal disc, growth is spatially homogeneous, the gradient scales and $g \approx \frac{1}{\beta}\frac{\dot{C}_0}{C_0}$ where $\beta \simeq 0.59$ is growth control parameter which has been previously estimated[2]. We then have,

$$0 = \frac{D_{eff}}{L^2} \partial_r^2 \tilde{C} - k_g \tilde{C} + s(r) \qquad \text{(S2.63)}$$

where $k_g = (k_{eff} + (1+\beta)g)$. A *quasi*-static approximation is valid if $k_{eff} \gg (1+\beta)g$ and the effects of growth on the decay length become negligible. We have measured the rates

k_{eff} and g (Extended Data Figures 4e and 2o, respectively). The measured values correspond to time scales of 39 minutes *versus* 25 hours in large discs and 15 minutes *versus* 20 hours in small discs, respectively. Therefore in both experimental conditions $k_{eff} \gg (1+\beta)g$ and so $k_g \approx k_{eff}$. In this case, scaling of the mobile pool gradient involves changes in k_{eff} (or D_{eff}) such that $D_{eff}/\, k_{eff}L^2$ remains constant and cannot be a result of growth effects.

We then asked how the decay length of the immobile pool evolves over time when the mobile pool scales as described above. Because $\tilde{C}(r,t) = C_0(t)\xi(r)$ has constant profile and only its amplitude varies in time, we can solve equation (S2.61) to obtain the following expression for $\widetilde{C_I}$

$$\widetilde{C_I}(r,t) = \bar{k}_i\, e^{-\left(k_2 t + \int_0^t dt'\, g(t)\right)} \int_0^t dt' \left(C_0(t) e^{\left(k_2 t + \int_0^t dt'\, g(t)\right)} \right) \xi(r) \qquad \text{(S2.64)}$$

It follows that if the profile of the mobile pool scales, the profile of the immobile pool also scales since only the amplitude of $\widetilde{C_I}$ (in red) varies with time and not $\xi(r)$. The total concentration satisfies

$$C_{tot} = C + C_I = \left(C_0(t) + \bar{k}_i\, e^{-\left(k_2 t + \int_0^t dt'\, g(t)\right)} \int_0^t dt' \left(C_0(t) e^{\left(k_2 t + \int_0^t dt'\, g(t)\right)} \right) \right) \xi(r) \qquad \text{(S2.65)}$$

We can therefore conclude that the immobile pool and total pool both have the same decay length as the mobile pool and scale with tissue size if the mobile pool scales. We confirm this conclusion experimentally (Extended Data 11h,i).

Note that the effective mobile pool in this analysis encompasses the three extracellular pools (L, S_R, S_L) and the mobile intracellular pool (S_e) employed in our analysis in the main text. It follows that the rate at which molecules move from the mobile to the immobile pool is an effective immobilization rate, not the same as k_i, explaining why the effective rate of immobilization, $\bar{k}_i$, was introduced.

This analysis reveals that, the immobile pool gradient is not reaching a steady state, but its decay length is set by the decay length of the mobile pool without delay and only the amplitude of the immobile pool gradient relaxes slowly with time.

In summary, the amplitude of the immobile pool relaxes slowly when the decay length of the mobile pool changes during scaling. In contrast, the decay length of the immobile pool follows instantaneously and expands to remain equal to the changing decay length of the mobile pool. This is consistent with our FRAP data described above showing that the decay length of the mobile pool is the same as the decay length of the total pool ($\lambda_T \simeq \lambda_M$, Extended Data

11h,i). Therefore dynamics of the decay length of the total pool scales during growth and reflects the changes of transport parameters which set the scaling decay length of the mobile pool.

3.10 Impact of morphogen leakage on the morphogen gradient formation

3.10.1 Impact of leakage on the decay length

In this section we consider the impact of loss of molecules in the extracellular space on the steady-state decay length. We introduce k_L, a rate that reflects the loss of molecules in the extracellular space due to leakage of molecules away from the tissue (or extracellular degradation). This introduces a change in the equations that capture the dynamics of our system so that the dynamics of the free extracellular molecules is now given by,

$$\frac{dL_n}{dt} = \frac{D_0}{a^2}(L_{n-1} - 2L_n + L_{n+1}) + k_{off}\left(S_n^{(r)} + S_{n+1}^{(l)}\right) - (k_{on}+k_L)L_n + \frac{1}{2}(\nu_n + \nu_{n+1}) \quad \text{(S2.66)}$$

Taking this into consideration, we derived the new characteristic polynomial of the system to obtain a new expression for the decay length given by,

$$\lambda^2 = \frac{1}{P_L}\left(\frac{D_0}{k_{on}} + \frac{D_0}{k_{on}}\frac{k_{off}}{k} + \frac{D_0}{k_{on}}\frac{k_{off}}{k}\frac{k_r}{k_i+k_1} + a^2\frac{k_r}{4(k_i+k_1)}\frac{k_{off}}{k_{off}+k}\right) \quad \text{(S2.67)}$$

where P_L is a leakage prefactor defined as,

$$P_L = 1 + k_L\left(\frac{1}{k_{on}} + \frac{k_{off}}{kk_{on}} + \frac{k_{off}k_r}{kk_{on}k_o}\right) \quad \text{(S2.68)}$$

For $k_L = 0$ equation (S2.67) becomes identical to equation (1) for the decay length used throughout our analysis. We can also obtain the ratio between the decay length with and without a leakage term as a function of the rate k_L given by $\left[\frac{\lambda(k_L=0)}{\lambda(k_L\neq 0)}\right]^2 = P_L$

It follows that if the rate k_L is small relative to the bracketed terms the change in the decay length due to loss of molecules in the extracellular space would be negligible. Our experiments with sGFP^{Dpp} and GFP-Dpp in chapter 2.11 indeed indicate that the leakage rate is negligible and that the effect of leakage is not important for the steady-state decay length.

3.10.2 Impact of leakage on parametrization

In order to assess to what extent does leakage impact our analysis, we repeated our parametrization procedure now using a theoretical framework that also considers leakage. To do this, we used the expression for the decay length derived in equation (S2.67), and added

a leakage term in the dynamics of the free extracellular pool when fitting the FRAP data (see above).

We have used the observation that sGFP^{Dpp} forms no detectable gradient away from its source (chapter 2.11.2) to estimate the upper bound for the leakage rate for Dpp $k_L < 0.0005\ s^{-1}$ (see chapter 2.11.2 for details). We have then determined the Dpp transport parameters assuming leakage rates around our estimated upper bound for $k_L = 0.00001\ s^{-1}, 0.0005\ s^{-1}$ and $0.001\ s^{-1}$ (Extended Data Figure 2i,j). These k_L values correspond to decay lengths of sGFP^{Dpp} of $\lambda = 2L, 3L$ and $6L$, respectively, with $L = 144.6\ \mu m$, target tissue length.

For all three values of k_L considered, we found that the estimated transport parameters of Dpp did not change noticeably (Extended Data Figure 2i). Furthermore, the contribution of the different modules to the decay length remained largely unchanged (Extended Data Figure 2j): recycling module dominates gradient formation for large discs.

Taken together, our analysis considering leakage of Dpp out of the epithelium shows that a low leakage rate of Dpp, as suggested by our experimental observations, is unlikely to have an impact on our parametrization and conclusions.

4 SUPPLEMENTARY DISCUSSION: Considerations of previously published data

4.1 Requirement of Pentagone for Dpp gradient scaling

A number of reports from different authors have addressed the question on the role of Pentagone on Dpp gradient formation. In the following chapter, we will particularly discuss the role of Pentagone in Dpp gradient scaling and the range of its activity.

Role of Pentagone in Dpp gradient scaling. In a number of previous reports[28-31], it has been show that, in *pentagone* mutants, the Dpp signaling gradient does not scale: the decay length of the P-Mad gradient does not increase with the increasing size of the wing disc. Note that in these reports, the *pentagone* mutant scaling phenotype has only been observed for signaling readouts (P-MAD[28-31], Dad[29], Spalt[29], Hairy[28]). In our report, we confirm the Pentagone-dependent scaling of the signaling gradient (Extended Data Figure 7b). Furthermore we show a scaling phenotype of the Dpp ligand gradient itself in *pent*^{2} mutants using eGFP-Dpp^{LOP} (Figure 2a; Extended Data Figure 7f).

Range of Pentagone activity. Previous reports show that Pentagone activity is non cell-autonomous and long-range. Indeed, an overexpansion of the Dpp gradient upon overexpression of Pentagone in one compartment (anterior or posterior) can be observed in both compartments (anterior and posterior), including the compartment where Pentagone has not been overexpressed[30,32].

Note that in Zhu *et al*., overexpression of Pentagone in clones causes a loss of Dpp signaling and it is cell-autonomous[31]. The result of this experiment in Zhu *et al*. is however inconsistent with observations in other reports: it is well established that loss of function *pentagone* mutants (not overexpression) reduce Dpp signaling, causing the range of the gradient to shrink[29,30,32], including the observations in Zhu *et al*.[31]. Indeed, overexpression of Pentagone causes a gain of function (*i.e*. expansion) Dpp signaling phenotype[30,32]. Moreover, our lab and other groups (manuscript submitted, not shown here) have repeated exactly the experiment in Zhu *et al*., which shows a different result: overexpression in clones shows a non-cell-autonomous gain of Dpp signalling (overexpanded decay length of the gradient), which is consistent with the previously published observations described above.

To support their claim that Pentagone acts short range and cell autonomously Zhu *et al.* looked at overexpressed Pentagone-GFP driven by Hedgehog-gal4, Apterus-gal4 and Cut-gal4 and argued that the spread from the source was short (their Figure 2A,A'). However, using the same reagents, we overexpressed Pentagone-GFP driven by Apterus-gal4 and observed that Pentagone is making a gradient with a substantially longer decay length than reported in Zhu *et al*. (see Extended Data Fig. 7d,e).

Despite some disagreement, together, most observations in different reports confirm that Pentagone activity is not cell-autonomous and long-range.

4.2 Importance of intracellular trafficking for Dpp gradient formation

To understand Dpp gradient scaling, we need to first understand how the gradient is formed. It is currently controversial which cellular transport phenomena are key to mediate Dpp spreading and gradient formation. Two alternative regimes of transport have been considered in the literature, where the key phenomena are different: a regime of pure extracellular diffusion plus receptor binding[9,25,33,34] *versus* a regime where there is a key role for intracellular endocytic transport[4,8,35,36].

4.2.1 Controversy in the literature

4.2.1.1 Interpretation of Dynamin-mutant clones

Using conditional endocytosis mutants and mosaic analysis, previous reports suggested that endocytosis and intracellular transport are important for morphogen gradient formation [4,8]. When GFP-Dpp is pulsed from its source, one can detect a wave of GFP-Dpp spreading throughout the wing (see Figure 5 in [8]). Thermosensitive *dynamin* mutant cell clones induced before the pulse cause the formation of "shadows" behind the clone where GFP-Dpp cannot be seen. This is a transient phenomenon. After a while, GFP-Dpp is seen behind the clone and the shadow disappears, because Dpp molecules can move in all directions and go around the clone. This indicates that Dpp requires endocytosis to spread in the tissue. A similar *shibire* clone experiment has been performed [33]. Here, clones were induced when the GFP-Dpp gradient was in steady state, and no shadows could be detected (see Figure 3 in [33]). This is consistent with theoretical work according to which such shadows would only be expected in the transient situation, off steady-state (see analysis of transient clones in [37]). An alternative theoretical work [38] suggests that shadow effects can occur even in steady state. These permanent effects however are much weaker than the transient effects and would therefore be very difficult to detect considering the noise in the experimental data.

4.2.1.2 FRAP vs FCS

Experiments of fluorescence recovery after photobleaching (FRAP) at the tissue level using GFP-Dpp ([4], see Figure 1D-L) were performed to estimate the effective diffusion and degradation. Because the recovery was slow, the effective diffusivity of Dpp in the wing was estimated to be much lower ($0.1\ \mu m^2 s^{-1}$) than that expected for molecules diffusing in aqueous solution (about $200\ \mu m^2 s^{-1}$). The observed low diffusivity is consistent with the time scales of slow cellular processes such as endocytosis, motor-driven motility of vesicular cargo, recycling, etc. These findings are compatible with a model in which Dpp molecules are endocytosed in cells and can recycle back to the extracellular space to contribute to the spreading of the morphogen [4,8,35,36]. Moreover, FRAP recovery curves in endocytosis-defective thermosensitive mutants of *dynamin* (see Figure 2 and S8 in [4]), where no recovery at the restrictive temperature was observed, confirm the importance of endocytic trafficking for Dpp transport.

In contrast, Fluorescence correlation spectroscopy (FCS), which measures the dynamics of molecules, has been used in the wing disc to estimate a rather fast extracellular diffusivity of Dpp ($20\ \mu m^2 s^{-1}$) [9]. A fast extracellular diffusivity and a rapid irreversible binding to receptors in the plasma membrane can in theory also account for the observed shape and decay length of gradients [9]. Consistently, in mammalian cultured cells, BMP2 binds rapidly (high k_{on}) and rather irreversibly (low k_{off}) to its signaling receptors [39,40].

The observed FRAP recovery dynamics of GFP-Dpp is therefore consistent with a regime where intracellular transport is relevant, but also with a regime where the gradient is formed by extracellular diffusion and irreversible receptor binding [9,25]. In an extracellular diffusion regime, the slow FRAP recovery is due to the internalization of morphogen molecules that accumulate slowly inside cells, without returning to the extracellular space. Note that this interpretation can however not account for the dynamin-mutant data (Figure 2 and S8 in [4]).

Because the existing data based on gradient decay length and FRAP recovery kinetics are compatible with both scenarios, we cannot currently exclude neither a regime of pure extracellular diffusion nor a regime where intracellular transport also contributes to gradient formation[1,9]. Additional information and assays are therefore essential to resolve the controversy. These additional assays are one of the focuses of the current report.

4.2.1.3 Dpp Photoconversion experiment

An experiment involving Dpp bound to a photoconvertible fluorophore Dendra2 contributed to the controversy described above [9]: following photoactivation in a region of interest (ROI) within the gradient, fluorescence spreading away from the photoactivated ROI was not detected (see Figure 2A-O in [9]). This is consistent with models of transport by free extracellular diffusion. In such models, only a small fraction of total Dpp (the extracellular molecules) participates in transport; the vast majority of Dpp molecules is trapped permanently on or within cells. In this extracellular diffusion model, most photoconverted molecules correspond to this intracellular immobile pool. Therefore, spread beyond the photoconverted region is not to be expected.

The lack of detected signal outside the photoactivated ROI can however be due to the fact that, in these experimental conditions, cells seem to have impaired ability to mobilize Dpp *i.e.* in the immobile fraction in this experiment is very large, in contrast to other reports ([4], the current report).

This is revealed when comparing the same experiment for Dpp and Wingless. Indeed, as a positive control of the Dpp photoactivation experiment, a Wingless–Dendra2 fusion protein was also used in that report. It has been previously shown (see Figure 3 in [4]) that GFP bound Wingless recovers fully in a FRAP experiment within 30 minutes following photobleaching of GFP: the immobile fraction of Wingless is negligible. The expected dynamics of build-up of photoactivated Wingless-Dendra2 within the configuration of the experiment (two photoactivated vertical stripes with a 10 µm distance between them) should be similar to the recovery dynamics in a FRAP experiment for Wingless-GFP: recovery between the two photoactivated stripes should be complete reflecting the absence of an immobile fraction. However only a mild increase of fluorescence outside of the photoactivated ROI could be observed in the photoconversion experiment for Wingless (see Figure 2P-Z in [9]). This indicates that there is a substantial immobile fraction for Wingless in this experiment, which might be caused by the experimental conditions. Therefore, the above mentioned photoconversion experiments have an impact in the mobility of intracellular molecules.

Consistently, the recovered fraction 30 minutes after FRAP photobleaching of GFP-Dpp in the work described above (i.e. the mobile fraction) is very small (20%; see Extended Data Figure 1J,M in [9]) compared to the mobile fraction we report here (45%; Extended Data Fig. 4b) and in a previous report (35%; see Figure 1D-L in Kicheva *et al*.[4]). This reflects the fact that the experimental conditions in the photoconversion experiment discussed above immobilize the intracellular Dpp molecules. It is therefore very likely that the very small pool of mobile Dpp molecules cannot be detected using this photoconversion experiment.

It is also worth noting that the nanobody photoconversion experiment presented in this work is fundamentally different. In our experiment, only the intracellular molecules are photoconverted by combining an internalization assay and acid wash to remove the extracellular nanobody molecule. Also, in our experimental setting the mobile fraction of molecules is large.

4.2.2 Theoretical study of the two extreme regimes of Dpp transport: ExD vs Tr

We have theoretically studied two extreme sets of parameter values: the set of parameter values considered in the literature which lead to the regime of Dpp spreading by pure extracellular diffusion [9], (ExD) and the set of parameter values for which only intracellular molecules contribute to spreading (Tr).

These two extreme regimes can be characterized using the four modules described in chapter 3.1. The three key parameters distinguishing these regimes are: D_0, k_{off} and k_r. The *ExD* regime is defined by a small or vanishing unbinding rate k_{off} and/or a negligible recycling rate k_{r} (Extended Data Fig. 1l). It is distinguished by the fact that intracellular molecules do not return to the diffusing extracellular pool. The ExD regime corresponds to scenarios where neither the "recycling module" nor the "transcytosis module" contribute to λ^2 (Extended Data Fig. 1k). In this case, only the extracellular pools are relevant to form the gradient: the bound module and/or unbound module are the relevant ones. This is akin to the model proposed in a number of reports [9,25,33,34]. In the other extreme, the Tr regime is defined by negligible extracellular diffusivity D_0 (Extended Data Fig. 1l). In this case, transport is mediated *via* recycling of the molecules in the intracellular pool and a "bucket brigade" of transport which was first proposed by Wolpert [26]. Here, only the "transcytosis module" contributes to λ^2 (Extended Data Fig. 1k).

There exist parameter values for these two scenarios that are compatible with both the observed decay length of the Dpp gradient and its dynamics of recovery in FRAP ([9]; Extended Data Fig. 1m,n). Therefore, the two assays available prior to the current work (FRAP and determination of the decay length in steady state) are not sufficient to address what is the actual mechanism of Dpp gradient formation.

4.2.3 Parameterisation of Dpp transport rates: ExD vs Tr

Is Dpp transported according to the ExD or Tr regimes described in the literature [9,26]? We showed above that three parameters distinguish diagnostically these two regimes: D_0, k_{off} and k_r. The experimental values for these rates obtained using our assays are intermediate between the values compatible with the ExD and Tr regimes discussed above (Extended Data Fig. 4l,m). The theoretical analysis (Extended Data Fig. 1k,l) shows that the Tr regime would require a large recycling rate to be compatible with both the FRAP recovery and the measured decay length of the gradient. Such large k_r values ($k_r \approx 0.75s^{-1}$) have never been reported for any cargo (reported k_r is around $10^{-3}s^{-1}$; [13,14]). Indeed, both the values of k_r reported and those measured here (Fig. 3a; Extended Data Table 1) are more than one-hundred fold smaller than $k_r \approx 0.75s^{-1}$ which is needed for the Tr regime (Extended Data Fig. 1l; 4l,m). Molecules should recycle within 1.3 seconds the k_r value of the Tr regime. This excludes pure Tr as a plausible regime. Furthermore, the measured value of D_0 is also too high to be

compatible with Tr (Extended Data Fig. 1l; 4l,m). The values of these parameters are also not compatible with the ExD regime proposed in the literature [9]: the values of D_0 and k_r lie between those characterizing ExD and Tr and the value of k_{off} is incompatible with ExD (Extended Data Fig. 1l; 4l,m).

4.3 Loss of Dpp from the extracellular space: leakage and degradation

In this chapter we evaluate the possibility of Dpp molecules to be lost from the extracellular space directly. This could potentially occur through two distinct mechanisms: leakage into the hemolymph and degradation in the extracellular space.

4.3.1 Leakage from the extracellular space.

A recent study[31] has explored the possible effects of molecular leakage in a synthetic system in the fly wing, providing interesting insights. Prompted by this study, we investigated the potential role of leakage of Dpp from the extracellular space of wing disc cells into the hemolymph. We found that leakage is not important. In order to study the importance of leakage, we have generated a secreted GFP construct (sGFP^{Dpp}), where the mRNA of secreted GFP is transcribed and the protein, translated, cleaved in the Golgi by Furin and secreted like Dpp (see Extended Data Figure 2c,d; chapter 2.11), unlike the Patched/Wingless-based secreted GFP in Stapornwongkul et al.[22]. Analysis of sGFP^{Dpp} shows that, when secreted like Dpp in the apical side, this molecule does not leak (Extended Data Figure 2c-h; see also chapter 2.11). We have then performed theoretical analysis where leakage is included in our 5 dynamic equations. This analysis shows that, with the leakage rate estimated for sGFP^{Dpp} (see chapter 2.11) our conclusions are not affected: the changes in the values of the different transport rates caused by considering leakage are negligible and the importance of the recycling module remains unaffected (chapter 3.10).

4.3.1.1 Secreted GFP leaks from the basal membrane in Stapornwongkul et al.[22]

In Stapornwongkul et al.[22], in the first part (their figures 1-3), the authors use secreted GFP which is detected as a gradient only when membrane bound nanobodies are present (no GFP gradient can be detected in the absence of those nanobodies); the authors observe an apical and a basal gradient with different properties. The authors then study gradient formation of the basal part only. There is an offset in this basal gradient, which the authors interpret as a signature of leakage. However, the basal gradient only represents 10% of the total signal: the

vast majority of the signal is apical. Note that no sign of leakage or offset is seen in the apical gradient.

In the second part of the report (their figures 4,5), signaling is studied. In this second part, the authors generate a Dpp signaling gradient synthetically based on GFP and an anti-GFP nanobody receptor which contains in this case a cytosolic tail taken from the actual Dpp receptors, Thickveins and Punt. Here the authors study signaling, but they cannot study gradient formation of the synthetic ligand. This is for three reasons:

i) In this scenario, the GFP gradient is not detectable (see Figure S10d-f in Stapornwongkul et al.[22]; "…note that no GFP gradient was detectable in this genetic background…"). Therefore, these experiments do not provide information about transport of these GFP molecules, the existence or not of offsets, the existence or not of leakage, or whether these molecules were internalized or not by endocytosis.

ii) If there is leakage in these conditions, as in the system in the first part of the Stapornwongkul et al.[22] report, the leaking pool would only be basal and represent only 10% of the total gradient. Instead, signaling could be elicited by the apical, non-leaking pool (the 90%). Therefore it is not known, whether only diffusion and leakage could generate the observed signaling gradient.

iii) The cytosolic tails of Thickveins and Punt in the rewired nanobody receptor are known to contain domains which elicit endocytosis and recycling. Therefore, endocytosis and recycling are expected to be mediated by these receptors and thus could be important for the intracellular trafficking of the GFP in the second part of this report (unlike the membrane bound nanobodies in the first part which lack those Thickveins/Punt domains).

4.3.1.2 $sGFP^{Ptc\text{-}Wg}$ versus $sGFP^{Dpp}$

It is well established, that in the wing epithelial cells, different membrane proteins (HSPGs vs. Notch vs. EGF, etc) traffic in the secretory pathway through different, non-overlapping populations of ER/Golgi organelles[41]. The targeting of these proteins to apical versus basal secretory compartments affects the location (apical vs basolateral) in which those molecules are secreted. The specific targeting of mRNA to a subset of ER/Golgi compartments is encoded in non-translated 5' and 3' UTR sequences in the mRNA as well as on signal peptide sequences at the protein level[42].

The reagent in the recent study by Stapornwongkul et al.[22] was generated by using the 5'UTR of *patched* fused to the coding region of the signal peptide of Wingless followed by the coding sequence of GFP downstream (we term this here sGFP$^{ptc\text{-}Wg}$). This construct is inserted in the endogenous *patched* gene and is therefore transcribed like *patched* (see scheme in Extended Data Figure 2c). The authors barely see sGFP$^{ptc\text{-}Wg}$ in the epithelium from what they conclude that these molecules are secreted basolaterally and leak basally into the hemolymph[22].

We have generated a transgenic fly using a Dpp cDNA where GFP is inserted into the Dpp coding sequence after the site of Furin cleavage in the Golgi, which separates the Dpp propeptide with its signal peptide (which remains in the Golgi apparatus of producing cells) and the C-terminal rest of the protein (the secreted ligand). In this construct, we engineered a STOP codon at the GFP C-terminus so that the mature peptide is not translated. Upon Furin cleavage, only GFP is produced (see scheme in Extended Data Figure 2d). Using the Gal4 system, we express it by means of a Dpp enhancer region. Therefore, this molecule (sGFP^{Dpp}) retains the 5'UTR of Dpp, the signal peptide of Dpp and the cleavage sites of Dpp followed by GFP: the mRNA of GFP is transcribed and the protein, translated, cleaved and traffics like Dpp. Note that there is no receptor that retains GFP at the membrane of the epithelial target cells and that GFP is not endocytosed as it is only present in the extracellular space: in this system there is only extracellular diffusion and, potentially, leakage. We have therefore generated a simplified system to study a potential role of leakage using a GFP molecule which shares with Dpp all the features of production, trafficking and secretion characteristics of the producing cells.

In chapter 2.11, we have already detailed how our data with sGFP^{Dpp} and GFP-Dpp are not consistent with a significant role of leakage for the formation of the Dpp gradient.

4.3.2 Extracellular degradation

Complete degradation of a protein occurs only by the proteasome or the lysosome inside cells. In fact, there is no indication that there is extracellular cleavage of Dpp itself (or any other BMP ligand in Drosophila or other species). Dpp is matured by Furin cleavage of a precursor in the trans-Golgi network and not the extracellular space. To date no proteases are known that can inactivate Dpp (or other BMPs) by cleavage extracellularly. Dpp signaling in the embryo is controlled by cleavage of the Dpp-binding protein Sog (but not Dpp itself) by the Tld protease. In any case, during imaginal disc patterning and growth in the larva, this

machinery does not function in Dpp spreading and signaling: mutants in this extracellular pathway (sog, Tsg, Tld, etc), which operates during dorso-ventral patterning in the embryo, do not show a Dpp signaling phenotype during larval phase and show only a later pupal function during the differentiation of veins. Therefore, there is no indication that extracellular cleavage of Dpp takes place in the wing.

4.4 Role of Thickveins in Dpp trafficking

Considering the unbinding rates reported in the literature for BMP and its receptor [39,40], the value we obtained for k_{off} was surprising (Fig. 3a). With the k_{off} values estimated in this report, bound molecules in the plasma membrane remain attached less than 25 seconds before they detach. If the receptor that endocytoses Dpp is the type I BMP receptor Thickveins (Tkv; [40]), then k_{off} is expected to be much smaller. Indeed, previous reports in mammals showed that the rate k_{off} of the type I BMP receptor for its BMP2 ligand is about $1.3 \cdot 10^{-3} s^{-1}$ corresponding to 800 seconds [40], which is more than one order of magnitude smaller than the one measured here. Similar arguments apply for the binding rate, which seems too low for a signaling receptor.

Moreover, we show that cells, mutant for tkv internalize GFP-Dpp^{LOP} normally. A similar result has been published previously[34]: removal of functional tkv, despite abolishing signal transduction activity, does not affect the Dpp gradient profile (see Figure 4 in [34]). Our data is therefore in line with previous reports to suggest that the Dpp signalling receptor Tkv is not the receptor which internalizes Dpp. As we propose in the current report, in order to signal, Dpp possibly encounters and binds Tkv in an intracellular compartment from where molecules do not return to the unbound extracellular pool. A similar scenario has recently been proposed for Wingless and its signaling receptor Frizzled in the wing [43] which do not bind in the plasma membrane, but can bind in an intracellular endosomal compartment, once the luminal pH has decreased.

It has been previously observed that overexpression of Thickveins in the wing imaginal disc does affect the range of the Dpp gradient as estimated by its activity (see Figure 3 in [44]): the range of the signalling gradient is decreased. This can be explained if dramatically increased levels of Tkv expression forces Dpp to bind Tkv along the endocytic pathways, at stages where pH is already low along the recycling route, thereby blocking Dpp in the recycling and spreading. The effect of Tkv on Dpp gradient formation would be an artefact of Tkv

overexpression, which puts together Dpp and Tkv in compartments where they would never meet in the wildtype condition.

4.5 Role of HSPGs in Dpp trafficking and Dpp gradient scaling

In Drosophila wing discs, two glypicans have been identified: Dally and Dally-like (Dlp). These are heparane sulfate proteoglycans (HSPGs) associated by a GPI-anchor to the outer leaflet of the plasma membrane. The involvement of these two glypicans in morphogen gradient formation and morphogen gradient signalling has been shown in a number of previous reports (reviewed in [22,45,46]).

4.5.1 Dally is involved on the scaling machinery of the Dpp gradient together with Pentagone

It was previously shown that *dally* mutations affect the range of the Dpp gradient ([47], see Figure 5). We show here that this phenotype is actually a scaling phenotype: in discs of increasing size, the gradient remains short, as seen both by looking at the Dpp ligand and the Dpp activity gradient (Extended Data Fig. 8a,b). Dally is therefore involved in Dpp gradient scaling.

Furthermore, we show that, as in *pentagone* mutants, the parameterization of transport rates in *dally* mutants confirms the absence of scaling by keeping D_0, k_{on} and k_{off} reduced and failing to engage the recycling module (Extended Data Fig. 8c,d). The scaling machinery which changes the binding properties of Dpp to engage recycling is therefore composed by Pentagone and Dally.

4.5.2 Dpp binding and unbinding rates (k_{on} and k_{off}) and the extracellular diffusivity D_0

In our theoretical framework, the Dpp binding and unbinding rates k_{on} and k_{off} describe the capture and release of Dpp by receptors at the plasma membrane that are responsible for subsequent Dpp internalization. Additional Dpp interactions with the membrane and the extracellular matrix components which do not lead to Dpp internalization underlie the extracellular diffusivity D_0. The value of D_0 is an effective extracellular diffusion coefficient which describes the diffusivity of the ligand and its binding/unbinding to molecules without subsequent endocytosis. Therefore, this effective D_0 could change if the interactions between Dpp and the cell membrane or extracellular matrix were altered.

Here we consider this relationship between the effective extracellular diffusivity and the extracellular diffusivity of unbound molecules (see also [48]). Let c be the total concentration of extracellular molecules and c_f and c_b the concentrations of free and extracellular molecules bound to molecules different to the internalization receptors which are immobile. The dynamics of c_f and c_b then obey,

$$\partial_t c_f = D_f \partial_x^2 c_f + K_{off} c_b - K_{on} c_f \quad \text{(S2.69)}$$

$$\partial_t c_b = K_{on} c_f - K_{off} c_b \quad \text{(S2.70)}$$

Where D_f is the diffusivity of unbound extracellular Dpp molecules and K_{on} and K_{off} are the binding and unbinding rates of Dpp to immobile molecules in the extracellular space which do not lead to internalization. At steady-state, $\partial_t c_b = 0$ and $c_b = \frac{K_{on}}{K_{off}} c_f$. The total concentration of extracellular Dpp molecules that are either free or bound to immobile components, c, satisfies

$$c = c_b + c_f = \left(1 + \frac{K_{on}}{K_{off}}\right) c_f \quad \text{(S2.71)}$$

The dynamics of c obey,

$$\begin{aligned} \partial_t c &= D_0 \partial_x^2 c \\ &= D_f \partial_x^2 c_f \\ &= D_f \partial_x^2 \left(\frac{1}{1 + K_{on}/K_{off}}\right) c \\ &= \left(\frac{1}{1+K_{on}/K_{off}}\right) D_f \partial_x^2 c \end{aligned} \quad \text{(S2.72)}$$

Where D_0 is the effective diffusivity of extracellular Dpp molecules that are either free or bound to immobile extracellular molecules as defined in this section and throughout this work. It follows that,

$$D_0 = \frac{D_f}{1+K_{on}/K_{off}} \quad \text{(S2.73)}$$

Equation (S2.73) shows that the effective extracellular diffusivity in the dynamical system of our analysis is smaller than the diffusivity of unbound extracellular molecules because of binding and unbinding of molecules to the extracellular matrix and non-internalizing receptors on the cell membrane. In principle, changes in these extracellular components can lead to changes in the effective extracellular diffusivity D_0. A similar derivation to the one presented here can also be found in [48].

4.5.3 How is D0 changed by Dally and Pentagone?

Pentagone binds Dally[32] and Dally binds Dpp[49] and could thereby potentially affect Dpp binding properties. In particular, Dally can act on Dpp by facilitating its diffusion in the extracellular matrix milieu (see Figure 8 in [47]). For example, Pentagone may facilitate binding of Dpp to Dally and thereby reduce the retention of Dpp by the extracellular matrix, which raises its extracellular diffusivity D_0 (see also chapter 4.5.2).

4.5.4 How does Pentagone and Dally affect the values of k_{on} and k_{off}?

The rates k_{on} and k_{off} describe the binding properties of the ligand to the receptor that mediates its internalization. GPI-anchor proteins can be internalized[43,50-54] and can therefore act as one of the internalization receptors which endocytose Dpp. One can speculate that, if Dally does function as one of the receptors which internalize Dpp, then the k_{on} and k_{off} rates that are regulated by Pentagone include the binding/unbinding rates of Dpp to Dally.

However, in the mutants for Pentagone or Dally, Dpp is still internalized. This implies that other receptors also contribute to Dpp internalization. Interestingly, it has been shown that in a double mutant for the two HSPG in the Drosophila genome, Dally and Dally-like (Dlp), the trafficking of Dpp is dramatically affected (Figure 6 in [33]).

This is consistent with a previous report, showing that trafficking of glypicans in the Drosophila wing is Pentagone-dependent[53]: in the absence of Pentagone, the internalization of glypicans is significantly reduced (see Figures 1(for Dally) and 2(for Dlp) in [53]).

In order to study whether Dally together with Dlp have an effect in Dpp endocytosis, we abolished both their function by downregulating Sulfateless expression in the posterior compartment through RNAi. Sulfateless is the enzyme that catalyzes the N-sulfation of the glucosamine in HSPGs, which is a prerequisite for heparane biosynthesis and therefore for HSPG production. We observed that Dpp internalization was dramatically affected upon Sulfateless silencing (see Extended Data Figure 8g-i).

If Dally and Dlp act as Dpp internalization receptors, it must be essential that these proteins are associated to the plasma membrane. To address this, we cleaved Dally and Dlp away from the plasma membrane by incubation with the PI-PLC enzyme. Under these conditions, we observed a considerable reduction of the Dpp endocytosis rate (see Extended Data Figure 8e,f).

These results indicate that together, Dally and Dlp might play a role as Dpp internalization receptors. Consistently, both *dally* and *sulfateless* mutants show a strong effect on the range of the Dpp gradient (Extended Data Figures 8h,i and 8a,b and reference[45]).

Interestingly, in Norman et al.[53] the authors also show that Thickveins trafficking is not affected in the absence of Pentagone (see Figure 3 in [53]). This is consistent with two of our observations in this report, namely that (i) Dpp trafficking is Pentagone-dependent and (ii) Thickveins is not the receptor that internalises Dpp.

4.5.5 How does Pentagone increase D_0, k_{on} and k_{off} during tissue growth to ensure scaling?

The process of gradient scaling involves an increase of D_0, k_{on} and k_{off} from small discs with short gradients to large discs with fully expanded gradients. Indeed, changes in decay length between small and large discs can be explained by a smooth and monotonous change in these three parameters (Extended Data Fig. 7a; see also chapter 3.8). How does Pentagone increase D_0, k_{on} and k_{off} during tissue growth to ensure scaling? The key lies in the increasing concentrations of Pentagone during tissue growth (Extended Data Fig. 7j,k) : in a large disc, large amounts of Pentagone would disengage Dpp from the extracellular matrix in a Dally-dependent manner, thereby increasing the effective D_0. In addition, Pentagone would also increase the k_{on} and k_{off} for Dally. The increase of Pentagone levels as the tissue grows can be ensured by the expansion-repression mechanism described in the literature[30,32]. This mechanism involves a feedback adjusting the size of the growing wing disc to the levels of Pentagone expression, controlled by Dpp signalling.

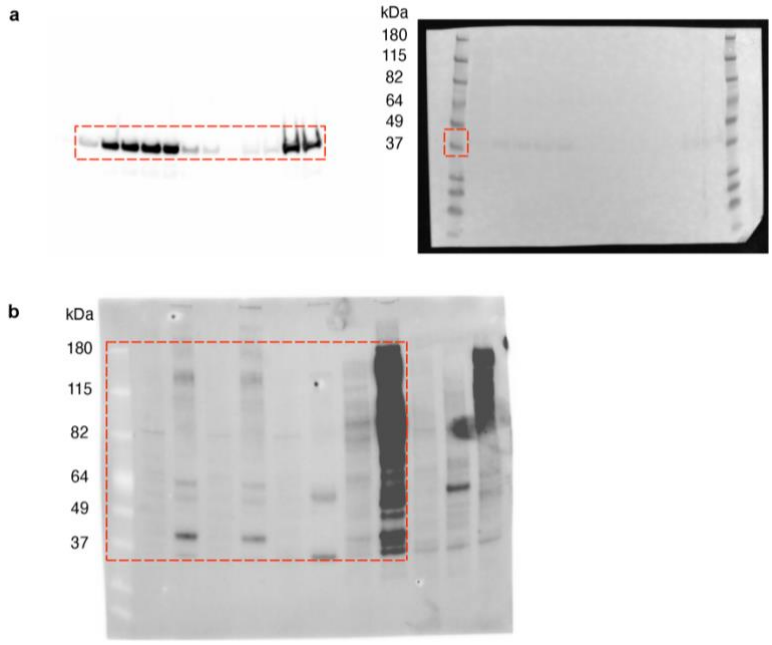

Supplementary Figure 1. Immunoblots. Full scan images of gels/blots corresponding to Extended Data Figures 1j **(a)** and 3a **(b)**.

CyO^{dpp+} *dpp-Gal4* *tkv^{8}* *EcadGFP* *hh-Gal4* *dally^{gem}*	described in flybase
dppLG *LOP-eGFP-Dpp*	[3]
UAS-sfGFP-mKate2-Dpp	described above (chapter 1.1.1)
eGFP-Dpp^{CRISPR}	described above (chapter 1.1.2)
UAS-GFP Pentagone	described above (chapter 1.1.3)
UAS-sGFP^{Dpp}	described above (chapter 1.1.4)
brk^{M68}	[34]
pent^{2}	[55]
UAS-GFP-Dpp	[8]
enGal4Gal80^{ts}	[8]
UAS-Rab4RNAi	VDRC ID2467
UAS-Rab11RNAi	VDRC ID22198
apGal4	[8]Bloomington Stock Center 3041
frgII-lacZ	[32]

Supplementary Table 1. Genotypes I. Description of used alleles.

Figure 1: a,b)	*Dpp-Gal4/UAS-eGFP-Dpp*
Figure 2,3	*LOP-eGFP-Dpp/+; dppLG/+* *$pent^2$, LOP-eGFP-Dpp /$pent^2$; dppLG /+*
Figure 4: a,b)	*hsFlp brk^{M68};$brk^{BACrescue}$,ubiGFP,FRT40/tkv^8,FRT40* *UAS-eGFP-Dpp/dpp-Gal4*
Figure 4: c-g)	*Dpp-Gal4/UAS-eGFP-Dpp*
Figure 4: h-o)	*Dpp-Gal4/UAS-sfGFP-mKate2-Dpp*
Extended Data Figure 1a-d	*Dpp-Gal4/UAS-eGFP-Dpp*
Extended Data Figure 1e-i	*LOP-eGFP-Dpp/+; dppLG/+*
Extended Data Figure 1j	*CyO-GFP/+*
Extended Data Figure 2a,b	*LOP-eGFP-Dpp/+; dppLG /+*
Extended Data Figure 2e-j	*UAS-$sGFP^{Dpp}$/+ ; Dpp-Gal4/+*
Extended Data Figure 2k-s	*LOP-eGFP-Dpp/+; dppLG/+*
Extended Data Figure 3a	*eGFP-Dpp^{CRISPR}/+* *eGFP-Dpp^{CRISPR}/CyO,Dpp^+* *LOP-eGFP-Dpp/+; dppLG/+* *Dpp-Gal4/UAS-sfGFP-mKate2-Dpp*
Extended Data Figure 3b-d	*LOP-eGFP-Dpp/+; dppLG, Dpp-Gal4/UAS-Dpp*
Extended Data Figure 3e-i	*LOP-eGFP-Dpp/+; dppLG/+* *$pent^2$, LOP-eGFP-Dpp /$pent^2$; dppLG /+*
Extended Data Figure 3j	*LOP-eGFP-Dpp/+; dppLG/+*
Extended Data Figure 3k-m	*LOP-eGFP-Dpp/+; dppLG/+* *$pent^2$, LOP-eGFP-Dpp /$pent^2$; dppLG /+*
Extended Data Figure 3o,p	*LOP-eGFP-Dpp/+; dppLG/+* *Oregon R*
Extended Data Figure 3q-t	*Oregon R*
Extended Data Figure 3u,v	*LOP-eGFP-Dpp/+; dppLG/+*
Extended Data Figure 4a,b	*LOP-eGFP-Dpp/+; dppLG/+* *$pent^2$, LOP-eGFP-Dpp /$pent^2$; dppLG /+*
Extended Data Figure 4c,d	*LOP-eGFP-Dpp/+; dppLG/+*

	pent^2, LOP-eGFP-Dpp /pent^2; dppLG /+
Extended Data Figure 4g,h	*LOP-eGFP-Dpp/+; dppLG/+* *pent^2, LOP-eGFP-Dpp /pent^2; dppLG /+*
Extended Data Figure 4i-k	*LOP-eGFP-Dpp/+; dppLG/+*
Extended Data Figure 4l,m	*LOP-eGFP-Dpp/+; dppLG/+* *pent^2, LOP-eGFP-Dpp /pent^2; dppLG /+*
Extended Data Figure 5a,b	*LOP-eGFP-Dpp/+; dppLG/+* *pent^2, LOP-eGFP-Dpp /pent^2; dppLG /+*
Extended Data Figure 5c-e	*LOP-eGFP-Dpp/+; dppLG/+* *pent^2, LOP-eGFP-Dpp /pent^2; dppLG /+*
Extended Data Figure 6a-f,h-j	*Dpp-Gal4/UAS-sfGFP-mKate2-Dpp*
Extended Data Figure 6g	*Oregon R*
Extended Data Figure 6k-o	*LOP-eGFP-Dpp/+; dppLG/+* *enGal4Gal80^{ts}/LOP-eGFP-Dpp; UAS-Rab11RNAi/ dppLG* *enGal4Gal80^{ts}/LOP-eGFP-Dpp; UAS-Rab4RNAi/ dppLG*
Extended Data Figure 6p-r	*LOP-eGFP-Dpp/+; dppLG/+*
Extended Data Figure 7c	*Oregon R* *pent^2/pent^2*
Extended Data Figure 7d,e	*ap-Gal4/UAS-GFP Pentagone*
Extended Data Figure 7f	*LOP-eGFP-Dpp/+; dppLG/+* *pent^2, LOP-eGFP-Dpp /pent^2; dppLG /+*
Extended Data Figure 7g-i	*LOP-eGFP-Dpp/+; dppLG/+* *pent^2, LOP-eGFP-Dpp /pent^2; dppLG /+*
Extended Data Figure 7j,k	*Pent-GFP MiMIC*
Extended Data Figure 8a	*Dpp-Gal4/UAS-eGFP-Dpp* *dally^{gem},Dpp-Gal4/dally^{gem},UAS-eGFP-Dpp*
Extended Data Figure 8b	*Oregon R* *dally^{gem}/dally^{gem}*
Extended Data Figure 8e,f	*Dpp-Gal4/ UAS-eGFP-Dpp*

	dally^{gem},Dpp-Gal4/dally^{gem},UAS-eGFP-Dpp
Extended Data Figure 8g-i	*eGFP-Dpp^{CRISPR}/CyO,Dpp^{+}* *eGFP-Dpp^{CRISPR}/CyO,Dpp^{+};UAS-sflRNAi/hh-Gal4* *Oregon R*
Extended Data Figure 8j-m	*LOP-eGFP-Dpp/+; dppLG* *eGFP-Dpp^{CRISPR}/CyO,Dpp^{+}*

Supplementary Table 2. Genotypes II. Detailed genotypes corresponding to experiments presented in main and Extended Data figures.

SUPPLEMENTARY REFERENCES

1 Aguilar Hidalgo, D., Hadjivasilou, Z., Romanova-Michaelides, M., González-Gaitán, M. & Jülicher, F. Dynamic modes of morphogen transport. arXiv:1909.13280 (2019). <https://ui.adsabs.harvard.edu/abs/2019arXiv190913280A>.

2 Wartlick, O. *et al.* Dynamics of Dpp signaling and proliferation control. *Science* **331**, 1154-1159, doi:10.1126/science.1200037 (2011).

3 Harmansa, S., Hamaratoglu, F., Affolter, M. & Caussinus, E. Dpp spreading is required for medial but not for lateral wing disc growth. *Nature* **527**, 317-322, doi:10.1038/nature15712 (2015).

4 Kicheva, A. *et al.* Kinetics of morphogen gradient formation. *Science* **315**, 521-525, doi:10.1126/science.1135774 (2007).

5 Durrieu, L. *et al.* Bicoid gradient formation mechanism and dynamics revealed by protein lifetime analysis. *Mol Syst Biol* **14**, e8355, doi:10.15252/msb.20188355 (2018).

6 Kirchhofer, A. *et al.* Modulation of protein properties in living cells using nanobodies. *Nat Struct Mol Biol* **17**, 133-138, doi:10.1038/nsmb.1727 (2010).

7 Derivery, E. *et al.* Polarized endosome dynamics by spindle asymmetry during asymmetric cell division. *Nature* **528**, 280-285, doi:10.1038/nature16443 (2015).

8 Entchev, E. V., Schwabedissen, A. & Gonzalez-Gaitan, M. Gradient formation of the TGF-beta homolog Dpp. *Cell* **103**, 981-991, doi:10.1016/s0092-8674(00)00200-2 (2000).

9 Zhou, S. *et al.* Free extracellular diffusion creates the Dpp morphogen gradient of the Drosophila wing disc. *Curr Biol* **22**, 668-675, doi:10.1016/j.cub.2012.02.065 (2012).

10 Kirchhausen, T., Owen, D. & Harrison, S. C. Molecular structure, function, and dynamics of clathrin-mediated membrane traffic. *Cold Spring Harb Perspect Biol* **6**, a016725, doi:10.1101/cshperspect.a016725 (2014).

11 Kural, C. *et al.* Dynamics of intracellular clathrin/AP1- and clathrin/AP3-containing carriers. *Cell Rep* **2**, 1111-1119, doi:10.1016/j.celrep.2012.09.025 (2012).

12 Sigismund, S. *et al.* Clathrin-mediated internalization is essential for sustained EGFR signaling but dispensable for degradation. *Dev Cell* **15**, 209-219, doi:10.1016/j.devcel.2008.06.012 (2008).

13 Felder, S., LaVin, J., Ullrich, A. & Schlessinger, J. Kinetics of binding, endocytosis, and recycling of EGF receptor mutants. *J Cell Biol* **117**, 203-212, doi:10.1083/jcb.117.1.203 (1992).

14 Waters, C. M., Oberg, K. C., Carpenter, G. & Overholser, K. A. Rate constants for binding, dissociation, and internalization of EGF: effect of receptor occupancy and ligand concentration. *Biochemistry* **29**, 3563-3569, doi:10.1021/bi00466a020 (1990).

15 Mineur, P. *et al.* Newly identified biologically active and proteolysis-resistant VEGF-A isoform VEGF111 is induced by genotoxic agents. *J Cell Biol* **179**, 1261-1273, doi:10.1083/jcb.200703052 (2007).

16 Wang, Y., Wang, X., Wohland, T. & Sampath, K. Extracellular interactions and ligand degradation shape the nodal morphogen gradient. *Elife* **5**, doi:10.7554/eLife.13879 (2016).

17 Khmelinskii, A. *et al.* Tandem fluorescent protein timers for in vivo analysis of protein dynamics. *Nat Biotechnol* **30**, 708-714, doi:10.1038/nbt.2281 (2012).

18 Aigouy, B., Umetsu, D. & Eaton, S. Segmentation and Quantitative Analysis of Epithelial Tissues. *Methods Mol Biol* **1478**, 227-239, doi:10.1007/978-1-4939-6371-3_13 (2016).
19 Roberts, T. M. *et al.* Identification and Characterisation of a pH-stable GFP. *Sci Rep* **6**, 28166, doi:10.1038/srep28166 (2016).
20 Shcherbo, D. *et al.* Far-red fluorescent tags for protein imaging in living tissues. *Biochem J* **418**, 567-574, doi:10.1042/BJ20081949 (2009).
21 Hu, Y. B., Dammer, E. B., Ren, R. J. & Wang, G. The endosomal-lysosomal system: from acidification and cargo sorting to neurodegeneration. *Transl Neurodegener* **4**, 18, doi:10.1186/s40035-015-0041-1 (2015).
22 Stapornwongkul, K. S., de Gennes, M., Cocconi, L., Salbreux, G. & Vincent, J. P. Patterning and growth control in vivo by an engineered GFP gradient. *Science* **370**, 321-327, doi:10.1126/science.abb8205 (2020).
23 Beckett, K. *et al.* Drosophila S2 cells secrete wingless on exosome-like vesicles but the wingless gradient forms independently of exosomes. *Traffic* **14**, 82-96, doi:10.1111/tra.12016 (2013).
24 de Madrid, B. H., Greenberg, L. & Hatini, V. RhoGAP68F controls transport of adhesion proteins in Rab4 endosomes to modulate epithelial morphogenesis of Drosophila leg discs. *Dev Biol* **399**, 283-295, doi:10.1016/j.ydbio.2015.01.004 (2015).
25 Lander, A. D., Nie, Q. & Wan, F. Y. Do morphogen gradients arise by diffusion? *Dev Cell* **2**, 785-796 (2002).
26 Wolpert, M. K. a. L. Mechanisms for Positional Signalling by Morphogen Transport: a Theoretical Study. *J. theor. Biol.* **191**, 103-114 (1998).
27 Fried, P. & Iber, D. Dynamic scaling of morphogen gradients on growing domains. *Nat Commun* **5**, 5077, doi:10.1038/ncomms6077 (2014).
28 Wartlick, O., Julicher, F. & Gonzalez-Gaitan, M. Growth control by a moving morphogen gradient during Drosophila eye development. *Development* **141**, 1884-1893, doi:10.1242/dev.105650 (2014).
29 Hamaratoglu, F., de Lachapelle, A. M., Pyrowolakis, G., Bergmann, S. & Affolter, M. Dpp signaling activity requires Pentagone to scale with tissue size in the growing Drosophila wing imaginal disc. *PLoS Biol* **9**, e1001182, doi:10.1371/journal.pbio.1001182 (2011).
30 Ben-Zvi, D., Pyrowolakis, G., Barkai, N. & Shilo, B. Z. Expansion-repression mechanism for scaling the Dpp activation gradient in Drosophila wing imaginal discs. *Curr Biol* **21**, 1391-1396, doi:10.1016/j.cub.2011.07.015 (2011).
31 Zhu, Y., Qiu, Y., Chen, W., Nie, Q. & Lander, A. D. Scaling a Dpp Morphogen Gradient through Feedback Control of Receptors and Co-receptors. *Dev Cell* **53**, 724-739 e714, doi:10.1016/j.devcel.2020.05.029 (2020).
32 Vuilleumier, R. *et al.* Control of Dpp morphogen signalling by a secreted feedback regulator. *Nat Cell Biol* **12**, 611-617, doi:10.1038/ncb2064 (2010).
33 Belenkaya, T. Y. *et al.* Drosophila Dpp morphogen movement is independent of dynamin-mediated endocytosis but regulated by the glypican members of heparan sulfate proteoglycans. *Cell* **119**, 231-244, doi:10.1016/j.cell.2004.09.031 (2004).
34 Schwank, G. *et al.* Formation of the long range Dpp morphogen gradient. *PLoS Biol* **9**, e1001111, doi:10.1371/journal.pbio.100111
10.1371/journal.pbio.1001111 (2011).

35 Bollenbach, T., Kruse, K., Pantazis, P., Gonzalez-Gaitan, M. & Julicher, F. Morphogen transport in epithelia. *Phys Rev E Stat Nonlin Soft Matter Phys* **75**, 011901, doi:10.1103/PhysRevE.75.011901 (2007).
36 Bollenbach, T., Kruse, K., Pantazis, P., Gonzalez-Gaitan, M. & Julicher, F. Robust formation of morphogen gradients. *Phys Rev Lett* **94**, 018103, doi:10.1103/PhysRevLett.94.018103 (2005).
37 Kruse, K., Pantazis, P., Bollenbach, T., Julicher, F. & Gonzalez-Gaitan, M. Dpp gradient formation by dynamin-dependent endocytosis: receptor trafficking and the diffusion model. *Development* **131**, 4843-4856, doi:10.1242/dev.01335 (2004).
38 Eldar, A. & Barkai, N. Interpreting clone-mediated perturbations of morphogen profiles. *Dev Biol* **278**, 203-207, doi:10.1016/j.ydbio.2004.11.002 (2005).
39 Allendorph, G. P., Isaacs, M. J., Kawakami, Y., Izpisua Belmonte, J. C. & Choe, S. BMP-3 and BMP-6 structures illuminate the nature of binding specificity with receptors. *Biochemistry* **46**, 12238-12247, doi:10.1021/bi700907k (2007).
40 Hatta, T. *et al.* Identification of the ligand-binding site of the BMP type IA receptor for BMP-4. *Biopolymers* **55**, 399-406, doi:10.1002/1097-0282(2000)55:5<399::AID-BIP1014>3.0.CO;2-9 (2000).
41 Yano, H. *et al.* Distinct functional units of the Golgi complex in Drosophila cells. *Proc Natl Acad Sci U S A* **102**, 13467-13472, doi:10.1073/pnas.0506681102 (2005).
42 Simmonds, A. J., dosSantos, G., Livne-Bar, I. & Krause, H. M. Apical localization of wingless transcripts is required for wingless signaling. *Cell* **105**, 197-207, doi:10.1016/s0092-8674(01)00311-7 (2001).
43 Hemalatha, A., Prabhakara, C. & Mayor, S. Endocytosis of Wingless via a dynamin-independent pathway is necessary for signaling in Drosophila wing discs. *Proc Natl Acad Sci U S A* **113**, E6993-E7002, doi:10.1073/pnas.1610565113 (2016).
44 Lecuit, T. & Cohen, S. M. Dpp receptor levels contribute to shaping the Dpp morphogen gradient in the Drosophila wing imaginal disc. *Development* **125**, 4901-4907 (1998).
45 Yan, D. & Lin, X. Shaping morphogen gradients by proteoglycans. *Cold Spring Harb Perspect Biol* **1**, a002493, doi:10.1101/cshperspect.a002493 (2009).
46 Takei, Y., Ozawa, Y., Sato, M., Watanabe, A. & Tabata, T. Three Drosophila EXT genes shape morphogen gradients through synthesis of heparan sulfate proteoglycans. *Development* **131**, 73-82, doi:10.1242/dev.00913 (2004).
47 Fujise, M. *et al.* Dally regulates Dpp morphogen gradient formation in the Drosophila wing. *Development* **130**, 1515-1522, doi:10.1242/dev.00379 (2003).
48 Morsdorf, D. & Muller, P. Tuning Protein Diffusivity with Membrane Tethers. *Biochemistry* **58**, 177-181, doi:10.1021/acs.biochem.8b01150 (2019).
49 Akiyama, T. *et al.* Dally regulates Dpp morphogen gradient formation by stabilizing Dpp on the cell surface. *Dev Biol* **313**, 408-419, doi:10.1016/j.ydbio.2007.10.035 (2008).
50 Guha, A., Sriram, V., Krishnan, K. S. & Mayor, S. Shibire mutations reveal distinct dynamin-independent and -dependent endocytic pathways in primary cultures of Drosophila hemocytes. *J Cell Sci* **116**, 3373-3386, doi:10.1242/jcs.00637 (2003).
51 Gupta, G. D. *et al.* Analysis of endocytic pathways in Drosophila cells reveals a conserved role for GBF1 in internalization via GEECs. *PLoS One* **4**, e6768, doi:10.1371/journal.pone.0006768 (2009).

52 Mayor, S., Parton, R. G. & Donaldson, J. G. Clathrin-independent pathways of endocytosis. *Cold Spring Harb Perspect Biol* **6**, doi:10.1101/cshperspect.a016758 (2014).
53 Norman, M., Vuilleumier, R., Springhorn, A., Gawlik, J. & Pyrowolakis, G. Pentagone internalises glypicans to fine-tune multiple signalling pathways. *Elife* **5**, doi:10.7554/eLife.13301 (2016).
54 Sabharanjak, S., Sharma, P., Parton, R. G. & Mayor, S. GPI-anchored proteins are delivered to recycling endosomes via a distinct cdc42-regulated, clathrin-independent pinocytic pathway. *Dev Cell* **2**, 411-423, doi:10.1016/s1534-5807(02)00145-4 (2002).
55 Vuilleumier, R., Affolter, M. & Pyrowolakis, G. Pentagone: patrolling BMP morphogen signaling. *Fly (Austin)* **5**, 210-214, doi:10.4161/fly.5.3.15311 (2011).